Collisional effects on electrostatic shock waves and heating in laser-generated plasmas

ANDRÉAS SUNDSTRÖM

Collisional effects on electrostatic shock waves and heating in laser-generated plasmas

ANDRÉAS SUNDSTRÖM

Cover:
Phase-space (constant-energy) contours of a model electrostatic shock distribution function. Blue dashed line represent the separatrix between the passing, reflected, trapped and co-propagating regions of phase space.

Collisional effects on electrostatic shock waves and heating in laser-generated plasmas

ANDRÉAS SUNDSTRÖM
Department of Physics
Chalmers University of Technology

Abstract

Electrostatic shock waves are associated with an electrostatic field structure propagating at supersonic speed through laboratory or astrophysical plasmas. Shock ion acceleration schemes, based on the strong electrostatic field in the shock structure, show promising potential due to the narrow energy spread of accelerated ions – which can be applied in plasma diagnostics, the generation of warm dense matter or medical purposes. The use of high-intensity laser pulses to generate shocks in the laboratory commonly result in plasmas which are weakly collisional; thus collisions are usually neglected in the corresponding theoretical, kinetic studies. By contrast, this thesis considers the effects of collisions on the structure and dynamics of electrostatic shocks as well as laser absorption and subsequent plasma heating.

First, the structure of electrostatic shocks is considered in weakly collisional plasmas, via a semi-analytical model. Collisions are found to cumulatively affect the shock structure on longer time scales, despite the low collisionality. Then, the impact of collisions on laser-driven plasmas is analyzed via numerical, particle-in-cell, simulations. The importance of collisions is heightened in plasmas comprising highly charged ions at solid density. Collisional inverse Bremsstrahlung heating is found to be able to generate well-thermalized electrons at energy densities relevant for warm- and hot-dense-matter applications. The strong electron heating also creates favorable conditions for electrostatic shocks. Collisions between shock-accelerated and upstream ions are found to increase the fraction of accelerated ions, thus bootstrapping the shock ion acceleration. Lastly, collisional ion heating is studied in connection to the shock. Different modeling approaches available to treat the highly collisional, solid density plasmas may predict qualitatively different shock dynamics, providing an opportunity for experimental model validation.

List of publications

A SUNDSTRÖM, A., JUNO, J., TENBARGE, J. M. & PUSZTAI, I. 2019 "Effect of a weak ion collisionality on the dynamics of kinetic electrostatic shocks". *Journal of Plasma Physics* **85**, 905850108,
DOI: [10.1017/S0022377819000023](10.1017/S0022377819000023)

B SUNDSTRÖM, A., SIMINOS, E., GREMILLET, L. & PUSZTAI, I. 2020*a* "Fast collisional electron heating and relaxation with circularly polarized ultraintense short-pulse laser". *Journal of Plasma Physics* **86**, 755860201,
DOI: [10.1017/S0022377820000264](10.1017/S0022377820000264)

C SUNDSTRÖM, A., SIMINOS, E., GREMILLET, L. & PUSZTAI, I. 2020*b* "Collisional effects on the ion dynamics in thin-foil targets driven by an ultraintense short pulse laser". *Plasma Physics and Controlled Fusion* **62**, 085015,
DOI: [10.1088/1361-6587/ab9a62](10.1088/1361-6587/ab9a62)

Acknowledgments

As this thesis marks the halfway point in my pursuits as a PhD student, it is high time I pause for moment to thank everyone who has made this possible. First and foremost, I have to gratefully thank István Pusztai, my supervisor, for supporting and guiding me through this dense underbrush of physical understanding and academic life. Next, I would also like to thank my co-supervisors Laurent Gremillet and Evangelos Siminos, they have both helped tremendously during the two last papers in this thesis. Laurent has been especially inexhaustible in giving comments and suggestions par excellence, which have undoubtedly improved my work in the last year. I must also thank the whole plasma theory group at Chalmers for being such good colleagues, and especially Tünde Fülöp for heading and managing to keep the group together – an excellent rock-star manager.

Lastly, I cannot but thank my friends and family, all of you! I want to especially thank my sister for many years of warm and, perhaps sometimes mischievous, friendship. A special thanks also goes out to hr. ing. Algehed for all the years of skookum fun and evenings of intense merriment.

<div style="text-align: right">Andréas Sundström, Göteborg, 2020-08-10</div>

Contents

Contents

Chapter 1

Introduction

Lasers have fascinated not only scientists, but the public in general. Early references in popular culture include the Bond film *Goldfinger* from 1964, in which the villain explains to Bond that the device which is pointing at him is a "*laser, which emits an extraordinary light, unknown in nature. It can project a spot on the moon. Or at closer range, cut through solid metal.*" This was only four years after the first demonstration of a working laser by Maiman in 1960. The laser portrayed in the film was pure science fiction at the time, but now, industrial lasers cutting metal are widely available, and already in 1973, the orbital distance of the Moon was measured using lasers (Bender *et al.*, 1973) – albeit with the help of retroreflectors left on the Moon as a part of the Apollo program.

Clearly, laser science has made tremendous progress the last 60 years. One of the crowning achievements in laser technology so far must have been the invention of the chirped pulse amplification (CPA) in 1985 by Strickland & Mourou, which was recognized with the 2018 Nobel prize in physics. CPA has allowed the creation of short-duration and extremely high intensity laser pulses, which have generated a vast range of applications at different levels of readiness, from already consumer-available laser eye surgery, to fundamental research topics such as basic laser–matter interaction at ever-increasing laser intensities.

At these high intensities, an irradiated target becomes exceedingly hot, and together with the strong electromagnetic fields from the laser, the atoms in the target may no longer be able to hold on to the electrons. The target material becomes ionized to a *plasma* state, which consists of a mixture of free electrons and ions. The presence of free charged particles – as opposed to atoms which are neutral – determines the nature of interaction between the laser electromagnetic fields and the target. The work outlined in this thesis concerns studying and modeling the interaction of such a high-intensity ($\sim 10^{20}\,\mathrm{W/cm^2}$) laser pulse with the target plasma, particularly in view of developing techniques for accelerating ions and creating warm dense matter using laser–plasma interactions.

1.1   Laser-based ion acceleration

One major envisioned application of high-intensity lasers is to utilize them for particle acceleration. Indeed, electron acceleration from laser irradiation was proposed

already in 1979 by Tajima & Dawson, and finally demonstrated experimentally by Amiranoff *et al.* (1998), based on a setup simulated by Joshi *et al.* (1984). Regarding the use of lasers to accelerate ions, Linlor (1963) reported observations of energetic ions only three years after the first laser, although the ∼keV energies are meager in contrast to current results. As laser technology improved, ion energies of ∼MeV were reported by Gitomer *et al.* (1986), using relatively long-duration (nanosecond) pulses, and by Fews *et al.* (1994), employing sub-picosecond, high-intensity laser pulses generated with CPA.

In more recent years, laser-accelerated ions have attracted considerable research attention – two reviews on the subject have been written by Daido, Nishiuchi & Pirozhkov (2012) and Macchi, Borghesi & Passoni (2013) – owing to the many envisioned or already demonstrated applications, many of which hinge upon the capacity of laser acceleration to produce a high number of ions in short-duration (picosecond) bunches. This feature makes laser-accelerated protons ideal for imaging of transient electromagnetic fields when the protons pass through plasmas (Borghesi *et al.*, 2002; Romagnani *et al.*, 2005), useful for diagnostic purposes. Such fast ions can also be used to generate *warm dense matter* – to be discussed in later chapters – when they irradiate and are absorbed in a target (Patel *et al.*, 2003; Dyer *et al.*, 2008; Mančić *et al.*, 2010). Laser-generated ions could also be used to produce neutrons through nuclear reactions (Roth *et al.*, 2013), which would be of a similarly short duration, not easily achievable otherwise by conventional means.

Another envisioned application of high energy ions is in ion-beam therapy. High-energy ions display a peculiar behavior that when they are used to irradiate matter, they deposit a large fraction of their energy at a well-defined depth, the so called Bragg peak. This feature makes ions particularly well suited for medical treatment, where, unlike photons or electrons, ions can be used to target tumors with limited damage to healthy surrounding tissue. The promise of laser-based ion accelerators here is in cost and availability (Bulanov *et al.*, 2002; Linz & Alonso, 2007) compared to conventional accelerators. While much scientific effort has been focused towards this goal, it is still beyond the current capabilities of laser-based accelerators. In order to become practical in medical use, the accelerators must be capable of producing particle energies of several hundred MeV per nucleon, at a very narrow energy spread and good repeatability (Giulietti & Tajima, 2016).

1.1.1 A brief overview of laser–plasma interactions

Plasmas consist of free charged particles, which all interact with, and generate their own, electromagnetic fields. The dynamics of the plasma is therefore closely linked with the electromagnetic fields present. The particles of the plasma may act collectively, giving rise to macroscopic fields, and they may interact microscopically, giving rise to *collisional effects* based on the practically random changes to individual particle trajectories. Since there are many competing effects in the plasma, the effects of collisions are at times insignificant to that of some other phenomena studied. Because of this, and due to the increased complexity required to model collisions, they are at times neglected. This work, however, has been focused on the effects of collisions in laser-plasma settings.

The problem of modeling the collective behavior of the plasma is very challenging, since the field and plasma interact non-linearly – the plasma generates its own fields which then affect the plasma. Yet, there are some simple principles which govern the basic field–plasma interactions. Since plasmas consist of free charged particles, they are very conductive, and low-frequency electric fields generally do not penetrate them very well. Static fields are shielded by the redistribution of charge in the plasma, known as *Debye shielding*. For oscillating fields, the plasma has a certain response rate, the *(electron) plasma frequency*, above which electromagnetic waves are transmitted. The plasma frequency depends on the *electron density* of the plasma – higher density gives a higher plasma frequency. So laser-plasmas are usually classified with respect to the laser frequency as either *overdense* or *underdense*, meaning that the plasma either reflects or (partially) transmits the laser light.

Besides oscillations induced by external fields, there is a whole plethora of different plasma waves, among which the *ion-acoustic wave* is of central importance to a key class of *electrostatic shocks*. The ion-acoustic wave propagates at a certain speed, simply called the *sound speed*, c_s, and that speed sets the limit for how fast (information about) a local perturbation to the ions can propagate to other parts of the plasma. If a strong enough perturbation is induced, such that it propagates faster than the sound speed, it will induce an ion-acoustic shock wave – some properties of which are studied in this thesis. Among these properties is the shock speed, usually expressed by the *Mach number*, $\mathcal{M} = v_{sh}/c_s$, which is the ratio of the shock speed to the sound speed (in the unperturbed plasma ahead of the shock front). Shocks are therefore characterized by a Mach number larger than unity, $\mathcal{M} > 1$.

1.1.2 Ion-acceleration mechanisms

In order to understand and develop laser-based ion acceleration, it is necessary to first understand the mechanisms by which ions are accelerated. To accelerate a particle, some force must act on it; in the case of a charged particle that force is provided by an electric field. The size of the accelerator is determined by the strength of the accelerating electric field together with the desired energy of the particles. In conventional accelerators, such as cyclotrons, synchrotrons and linear accelerators, that electric field is supplied as a high-power radio-frequency (RF) electromagnetic wave. In such devices, the electric field strength is not only limited by the RF power available, but also the material properties of the accelerator chambers – i.e. limitations on how strong fields they can withstand without damage due to electrical breakdown. Typically, the field strength of conventional RF accelerators is limited to $\lesssim 0.1\,\mathrm{GV/m}$, which means that these accelerators operate on macroscopic (meter) scales.

The accelerating structures in laser-based accelerators, on the other hand, are not limited by material damage thresholds. Since the material (a plasma) is already ionized, damage due to breakdown is no longer relevant. Therefore, laser-plasma accelerators can operate on a microscopic scale, thanks to the accelerating fields reaching as strong as $\sim\mathrm{GV/m}$ (Litos *et al.*, 2014) or even $\sim\mathrm{TV/m}$ (Higginson *et al.*, 2018), depending on the acceleration scheme. Below, three of the more common laser-based ion-acceleration mechanisms are presented briefly.

Target normal sheath acceleration

One of the simplest, and most robustly observed, ion acceleration mechanisms is the *target normal sheath acceleration* (TNSA) first described by Wilks *et al.* (2001). In short, it relies on first energizing part of the target electrons with the laser; the high-energy electrons will then tend to escape from the target, thus creating positively charged sheaths at the plasma–vacuum boundaries, which produces a strong electrostatic field directed outward from the plasma. This field acts to reflect the electrons back into the target, while accelerating the surface ions. The laser energy, first converted into electron kinetic energy, is then eventually transferred to the target ions. Although this mechanism is rather robust and generally produce the largest number of accelerated ions in laser ion-accelerators, TNSA typically produce broad ion energy spectra, exponentially decreasing over several orders of magnitude. Such large energy spread can be detrimental to applications that require well-defined ion energies.

Since TNSA relies on the production of high-energy electrons before the ions are accelerated, low-density targets are generally preferable. This is because the penetration depth of the laser depends on the density of the plasma. The deeper the laser penetrates, the larger fraction of the electrons it can energize, and thus the stronger the sheath field will become. Recent experiments by Higginson *et al.* (2018) yielded protons at a maximum energy of 94 MeV, utilizing relativistic transparency (Kaw & Dawson, 1970) – to be discussed, in brief, later – in order to have deep laser penetration.

Radiation pressure acceleration

Another ion-acceleration mechanism whose mechanism can easily be grasped is *radiation pressure acceleration* (RPA). The concept that electromagnetic radiation can exert a force on matter has been known for over a century (Lebedew, 1901), and may be understood either classically or quantum mechanically by the momentum carried by the electromagnetic wave or by the photons, respectively. Esirkepov *et al.* (2004) proposed that this pressure may also be suitable to accelerate accelerate ultra-thin targets as a whole. This mechanism is sometimes referred to as *light sail acceleration* (Macchi, 2014). Since radiation pressure is only exerted by absorbed or reflected radiation, it occurs only in plasmas opaque to to the laser light.

Although simple in theory, RPA is limited by the deformation of the plasma due to transverse instabilities. As an example, if there is any small variation in plasma density, the inertial mass resisting acceleration would be varying correspondingly. Regions with lower density will be pushed more effectively, and some of the plasma will even be pushed to the side, thus amplifying the density variation. Through this process, a hole may be formed in the light sail, through which the light may "leak" to the detriment of the ion acceleration. The light sail may also be destroyed by relativistic transparency (Kaw & Dawson, 1970), which severely decreases the effectiveness for further RPA. Recent experiments by Kim *et al.* (2016) have, however, reported radiation pressure accelerated protons up to 93 MeV.

Collisionless shock acceleration

The last ion-acceleration mechanism discussed here is called *collisionless shock acceleration* (CSA), described as early as in the sixties by Moiseev & Sagdeev ([1963]). It is a slightly more involved concept in terms of the acceleration mechanism. Through the impact of the laser pulse, a shock wave is generated which propagates at a (moderately) supersonic speed through the plasma. In a weakly or non-collisional plasma, the shock front consists of a very steep density gradient (of the order of the Debye length), associated with a sharp electrostatic field capable of reflecting part of the upstream ions. The reflected ions reach speeds up to twice the speed of the shock – similarly to how a golf ball bounces off the golf club at roughly twice the club's velocity. Given the right conditions, the shock may propagate through the plasma, continuously accelerating ions to the same speed, thus generating a fairly monoenergetic accelerated ion population. The low spread in accelerated ion energies is also what makes CSA an interesting alternative to TNSA, for certain applications.

The first simulation study of electrostatic collisionless shocks was performed by Forslund & Shonk ([1970]). Later numerical investigations, such as those by Denavit ([1992]), Silva *et al.* ([2004]) and Fiuza *et al.* ([2012]), investigated the shock formation due the impact of a laser pulse. CSA has recently seen experimental confirmation in various settings (Romagnani *et al.*, [2008]; Haberberger *et al.*, [2012]; Zhang *et al.*, [2017]; Antici *et al.*, [2017]; Pak *et al.*, [2018]). However, due to the more complicated nature of shock waves, particularly with regards to shock formation and stability, the currently highest proton energy reported from CSA is $\sim 45\,\mathrm{MeV}$ from the experiment by Antici *et al.* ([2017]), which is significantly lower than the maximum energies reported for TNSA or RPA, and also lower than the requirement for medical use in ion-beam therapy. Still, the nearly monoenergetic spectrum of shock-accelerated ions is in favor for CSA to be used in ion-beam therapy.

Besides the applications directly related to ion acceleration in laboratory settings, collisionless shocks are also ubiquitous in astrophysical plasmas (Lee, Mewaldt & Giacalone, [2012]). Although astrophysical shocks are usually mediated by a finite ambient or self-generated magnetic field, they may bear resemblance, in certain respects, to the essentially electrostatic shock arising in laser–plasma interactions (Dieckmann *et al.*, [2017]).

1.2 Warm-dense-matter generation

Besides the relatively application-oriented field of laser-plasma based acceleration, laser-generated plasmas can also be of interest to basic research fields, such as the study of *warm/hot dense matter* (W/HDM). These states of matter are, as the name suggests, characterized by a high temperature (> 1 million kelvin) and at the same time high density (comparable to the density of solids). Another way of saying this is that the pressure is extremely high (reaching up to billions of times the atmospheric pressure). Currently, we do not have a full understanding of the behavior of matter under these extreme conditions. There is therefore a need to be able to create and study W/HDM in the laboratory.

While reaching *either* high temperature *or* high density can generally be done, achieving both simultaneously is harder to do in a controlled environment. As an example, temperatures of tens of keV ($\sim 10^8$ K) are regularly reached in magnetic confinement fusion experiments, but the particle densities are of the order of $\sim 10^{14}$ particles per cubic centimeter (cm^{-3}) – as a comparison, the number density of air at room temperature (25 meV) and atmospheric pressure is about $\sim 2.5 \times 10^{19}$ cm^{-3}. Conversely, similarly high temperatures, at a much higher density, are reached in the detonation of a thermonuclear weapon (commonly known as a "hydrogen bomb"), but that can hardly be considered a controlled nor safe environment for W/HDM experiments. The problem is, as mentioned, that the pressure becomes exceedingly high when both the temperature and density are high.

By employing lasers, large amounts of energy can be delivered to a small volume of matter, allowing it to be *isochorically* heated, i.e. heated faster than the plasma can expand. This technique for creating W/HDM in a laboratory setting can be used in a broad range of research disciplines such as laboratory astrophysics (Remington *et al.*, 1999; Remington, 2005; Bailey *et al.*, 2007; Fujioka *et al.*, 2009), and studies of planetary interiors (Ross, 1981; Knudson, Desjarlais & Dolan, 2008). The goal of these studies is to emulate the extreme conditions that matter is subjected to in some astrophysical events, e.g. supernovae explosions, or the enormous pressures found in the cores of stars and planets. Knowledge of how matter behaves at these pressures would benefit the broader understanding of such phenomena and help constrain stellar and planetary evolution models. This knowledge includes understanding the equations of state under these extreme conditions (Renaudin *et al.*, 2003; Nettelmann *et al.*, 2008), i.e. how temperature and pressure are related, and experimental verification of high-energy-density (HED) atomic physics models (Hoarty *et al.*, 2013*a*; Faussurier & Blancard, 2019). Fast heating with compression by laser irradiation is also the building block of inertial confinement fusion (Le Pape *et al.*, 2018; Drake, 2018), which aims at heating and compressing sufficiently to cause hydrogen nuclei to fuse together and release energy – akin to a thermonuclear weapon, although on a much smaller scale.

Isochorically heating a plasma with lasers is not a trivial task. Since a high-density plasma is generally reflective to light, the absorbed fraction of the laser energy into plasma is of the order of a few percent only. However, even though laser-based isochoric heating is challenging, there has been several successful such experiments on powerful ($0.1-1$ PW), high-intensity ($>10^{18}$ W cm^{-2}) laser systems (Evans *et al.*, 2005; Gregori *et al.*, 2005; Martinolli *et al.*, 2006; Chen *et al.*, 2007; Nilson *et al.*, 2009; Pérez *et al.*, 2010; Brown *et al.*, 2011; Hoarty *et al.*, 2013*b*). Recently, there have also been results by Purvis *et al.* (2013) and Bargsten *et al.* (2017), making use of nano-wire arrays to strongly enhance the laser-to-plasma coupling efficiency, thus creating keV-temperature plasmas with a smaller-scale laser system.

1.3   Outline

In this thesis, we will explore some aspects of shock acceleration and laser-driven plasma heating, in particular how these processes might be affected when considering inter-particle collisions. We first lay down a theoretical base for the kinetic modeling

of plasmas in chapter 2; here we will also spend some time on the modeling of collisions (§ 2.2) as well as how kinetic theory is translated to numerical simulation methods (§§ 2.3 and 2.4).

From these fundamentals, we will study the interaction between the laser and the plasma in order to discuss the effects of collisions on the electron heating and electrostatic shocks. Chapter 3 starts with a review of the basic theory of electromagnetic waves and how they interact with particles and plasmas (§ 3.1), and a discussion on plasma heating (§§ 3.2 and 3.3). This is followed by a discussion on collisional effects on electrostatic shocks, both in weakly collisional plasmas (§ 3.4.1), with a semi-analytical model for electrostatic shocks, and in more strongly collisional plasmas by studying particle-in-cell simulations of such scenarios (§ 3.4.2). The main body of the thesis ends on chapter 4, with a summary of the enclosed papers and a brief outlook on potential extensions of the work in said papers.

Chapter 2

Kinetic modeling of plasmas

To fully describe a plasma, we would, in principle (hypothetically), like to solve the equations of motion for all the particles and their interactions with each other through the electric, $\tilde{\boldsymbol{E}}$, and magnetic, $\tilde{\boldsymbol{B}}$, fields (the 'tilde' denotes an exact quantity on the microscopic level). This is done, ignoring quantum effects, by first introducing the equations of motion with the Lorentz force acting on a charge particle in an electromagnetic field

$$\frac{\mathrm{d}\tilde{\boldsymbol{p}}_{i_a}}{\mathrm{d}t} = eZ_a^*\Big[\tilde{\boldsymbol{E}}(\tilde{\boldsymbol{r}}_{i_a}, t) + \tilde{\boldsymbol{v}}_{i_a} \times \tilde{\boldsymbol{B}}(\tilde{\boldsymbol{r}}_{i_a}, t)\Big], \tag{2.1}$$

where $\tilde{\boldsymbol{p}}_{i_a}$ is the momentum of particle i_a, belonging to species a (e.g., electrons or ions, denoted by $a = \mathrm{e}$ and $a = \mathrm{i}$, respectively), and $\tilde{\boldsymbol{v}}_{i_a} = \mathrm{d}\tilde{\boldsymbol{r}}_{i_a}/\mathrm{d}t$ is its velocity; eZ_a^* is the charge of a particle of species a, in terms of the *charge number* of the species, Z_a^* ($Z_\mathrm{e}^* = -1$ for electrons), and the elementary charge, $e \approx 1.6 \times 10^{-19}$ C. As the energy of a particle may become large compared to its rest energy, $m_a c^2$, a relativistic formulation is necessary, i.e. $\tilde{\boldsymbol{p}}_{i_a} = \tilde{\gamma}_{i_a} m_a \tilde{\boldsymbol{v}}_{i_a}$ with $\tilde{\gamma}_{i_a} = [1 + (\tilde{p}_{i_a}/m_a c)^2]^{1/2} = [1 - (\tilde{v}_{i_a}/c)^2]^{-1/2}$, where m_a is the rest mass of a particle of species a, and c is the speed of light in vacuum.

Then, the electric and magnetic fields are governed by Maxwell's (1865) equations (in the *SI convention* for electromagnetism),

$$\begin{aligned}\boldsymbol{\nabla} \cdot \tilde{\boldsymbol{E}} = \frac{\tilde{\rho}}{\epsilon_0}, \qquad &\boldsymbol{\nabla} \times \tilde{\boldsymbol{E}} = -\frac{\partial \tilde{\boldsymbol{B}}}{\partial t} \\ \boldsymbol{\nabla} \cdot \tilde{\boldsymbol{B}} = 0, \qquad &\boldsymbol{\nabla} \times \tilde{\boldsymbol{B}} = \mu_0 \tilde{\boldsymbol{j}} + \mu_0 \epsilon_0 \frac{\partial \tilde{\boldsymbol{E}}}{\partial t},\end{aligned} \tag{2.2}$$

where the charge and current densities are given by the sum of the contributions from every particle

$$\begin{aligned}\tilde{\rho}(\boldsymbol{r}, t) &= \sum_a q_a \sum_{i_a} \delta\Big(\boldsymbol{r} - \tilde{\boldsymbol{r}}_{i_a}(t)\Big), \\ \tilde{\boldsymbol{j}}(\boldsymbol{r}, t) &= \sum_a q_a \sum_{i_a} \tilde{\boldsymbol{v}}_{i_a}(t)\, \delta\Big(\boldsymbol{r} - \tilde{\boldsymbol{r}}_{i_a}(t)\Big),\end{aligned} \tag{2.3}$$

which couples back to the individual equations of motions (2.1). The summations are performed over all plasma species, a, and the individual particles of that species,

i_a. The Dirac delta function, δ, is used here to represent the point-like nature that the particles are assumed to have.

The problem, however, is that the indices i_a hide an enormous number of particles involved. In a typical laser-plasma experiment, where the typical plasma volumes are rather small, the number of particles might be as large as in the order of 10^{15} particles involved in the plasma. Needless to say, that is too many equations to integrate and too much information to process in practice. Some method must therefore be devised in order to reduce the size of the problem.

2.1 Kinetic theory

One way to make the problem tractable while still, to a degree, preserving effects of individual particle dynamics, is through *kinetic theory*. Kinetic theory is based on statistical mechanics, wherein a physical system is described with the help of a (statistical) distribution of particles in *phase space*, which encompasses both a (real or configuration) spatial coordinate, $\boldsymbol{r}$, and a momentum coordinate, $\boldsymbol{p}$. There are, however, other possibilities for modeling a plasma, such as with a fluid theory, where the plasma is modeled as one or more fluids which interact electromagnetically. While a fluid theory further reduces the complexity of the problem, it also lacks the modeling power afforded by retaining both the configuration and momentum spaces, which kinetic theory provides. There might, for instance, be two populations of the same species of particles but with different momenta, e.g. a beam of fast particles moving through a background population; this will easily be captured by kinetic theory, while a fluid theory would struggle to capture the nature of the two distinct populations – unless with an artificial division of the two populations into two separate fluids.

A first step toward a kinetic description is to introduce a microscopic distribution function, generally known as the *Klimontovich distribution function* (1967),

$$\tilde{f}_a(\boldsymbol{r}, \boldsymbol{p}; t) = \sum_{i_a} \delta\Big(\boldsymbol{r} - \tilde{\boldsymbol{r}}_{i_a}(t)\Big)\delta\Big(\boldsymbol{p} - \tilde{\boldsymbol{p}}_{i_a}(t)\Big), \tag{2.4}$$

where $[\boldsymbol{r}, \boldsymbol{p}]$ are coordinates in phase space. This distribution describes the positions of all particles of species a in phase space. In order to write an equation for the time evolution of the system, we need to find the derivative of $\tilde{f}_a$ with respect to time:

$$\begin{aligned}
\frac{\partial \tilde{f}_a}{\partial t} &= \sum_{i_a} \frac{\partial}{\partial t}\Big[\delta\Big(\boldsymbol{r} - \tilde{\boldsymbol{r}}_{i_a}(t)\Big)\delta\Big(\boldsymbol{p} - \tilde{\boldsymbol{p}}_{i_a}(t)\Big)\Big] \\
&= \sum_{i_a} \left\{ \frac{\partial}{\partial \tilde{\boldsymbol{r}}_{i_a}}[\delta(\boldsymbol{r}-\tilde{\boldsymbol{r}}_{i_a})] \cdot \frac{\mathrm{d}\tilde{\boldsymbol{r}}_{i_a}}{\mathrm{d}t}\delta(\boldsymbol{p}-\tilde{\boldsymbol{p}}_{i_a}) \;+\; \delta(\boldsymbol{r}-\tilde{\boldsymbol{r}}_{i_a})\frac{\partial}{\partial \tilde{\boldsymbol{p}}_{i_a}}\Big[\delta(\boldsymbol{p}-\tilde{\boldsymbol{p}}_{i_a})\Big] \cdot \frac{\mathrm{d}\tilde{\boldsymbol{p}}_{i_a}}{\mathrm{d}t} \right\} \\
&= \sum_{i_a} \left\{ \frac{\partial \tilde{f}_a}{\partial \tilde{\boldsymbol{r}}_{i_a}} \cdot \tilde{\boldsymbol{v}}_{i_a} + \frac{\partial \tilde{f}_a}{\partial \tilde{\boldsymbol{p}}_{i_a}} \cdot \dot{\tilde{\boldsymbol{p}}}_{i_a} \right\},
\end{aligned} \tag{2.5}$$

where $\dot{\tilde{\boldsymbol{p}}}_{i_a} = \mathrm{d}\tilde{\boldsymbol{p}}_{i_a}\big/\mathrm{d}t$ is given by (2.1), and differentiation with respect to a vector is to be viewed as a gradient. Note that processes which can alter the number

of particles of a specific species, such as ionization/recombination, are ignored for the moment. The next nuance is to conclude that since $\tilde{f}_{i_a}$ only consists of delta-functions, $\tilde{\boldsymbol{v}}_{i_a}$ and $\dot{\tilde{\boldsymbol{p}}}_{i_a}$ may be replaced by their representations with phase-space coordinates[*] $\tilde{\boldsymbol{v}}$ and $\dot{\tilde{\boldsymbol{p}}}$ (without the indices i_a). These coordinates can then be lifted outside the sum, giving

$$\frac{\partial \tilde{f}_a}{\partial t} = \tilde{\boldsymbol{v}} \cdot \sum_{i_a} \frac{\partial \tilde{f}_a}{\partial \tilde{\boldsymbol{r}}_{i_a}} + \dot{\tilde{\boldsymbol{p}}} \cdot \sum_{i_a} \frac{\partial \tilde{f}_a}{\partial \tilde{\boldsymbol{p}}_{i_a}}. \tag{2.6}$$

From the definition of $\tilde{f}_a$ in (2.4), it follows that

$$\sum_{i_a} \frac{\partial \tilde{f}_a}{\partial \tilde{\boldsymbol{r}}_{i_a}} = -\frac{\partial \tilde{f}_a}{\partial \boldsymbol{r}} \quad \text{and} \quad \sum_{i_a} \frac{\partial \tilde{f}_a}{\partial \tilde{\boldsymbol{p}}_{i_a}} = -\frac{\partial \tilde{f}_a}{\partial \boldsymbol{p}}, \tag{2.7}$$

which finally gives the Klimontovich equation

$$\frac{\partial \tilde{f}_a}{\partial t} + \boldsymbol{v} \cdot \frac{\partial \tilde{f}_a}{\partial \boldsymbol{r}} + Z_a^* \tilde{\boldsymbol{K}} \cdot \frac{\partial \tilde{f}_a}{\partial \boldsymbol{p}} = \frac{\mathrm{d}\tilde{f}_a}{\mathrm{d}t} = 0, \tag{2.8}$$

where

$$\tilde{\boldsymbol{K}} = \tilde{\boldsymbol{K}}(\boldsymbol{r}, \boldsymbol{v}; t) = \frac{\dot{\tilde{\boldsymbol{p}}}}{Z_a^*} = e[\tilde{\boldsymbol{E}}(\boldsymbol{r}, t) + \boldsymbol{v} \times \tilde{\boldsymbol{B}}(\boldsymbol{r}, t)] \tag{2.9}$$

is introduced to represent the Lorentz force acting on a particle of charge e. (In general, however, $Z_a^* \tilde{\boldsymbol{K}}$ may be extended to represent any net force, e.g. gravity, acting on a test particle of species a at time t and position $\boldsymbol{r}$.) The Klimontovich equation is a special case of Liouville's theorem for statistical dynamics, which sates that a phase-space distribution function of a system governed by Hamiltonian mechanics remains constant along any phase-space trajectory, i.e. $\mathrm{d}\tilde{f}/\mathrm{d}t = 0$.

The evolution of the system is now described by (2.8), together with Maxwell's equations (2.2) and the extension of the charge and current densities in (2.3),

$$\tilde{\rho}(\boldsymbol{r}, t) = \sum_a q_a \int \mathrm{d}^3 p' \, \tilde{f}_a(\boldsymbol{r}, \boldsymbol{p}'; t),$$
$$\tilde{\boldsymbol{j}}(\boldsymbol{r}, t) = \sum_a q_a \int \mathrm{d}^3 p' \, \boldsymbol{v}' \tilde{f}_a(\boldsymbol{r}, \boldsymbol{p}'; t). \tag{2.10}$$

So far, however, little has changed in terms of complexity. There are still $6N_a$ unknown variables behind $\tilde{\boldsymbol{r}}_{i_a}$ and $\tilde{\boldsymbol{p}}_{i_a}$, where N_a is the number of particles of species a. So for transparency, $\tilde{f}_a$ should really be written as $\tilde{f}_a(\boldsymbol{r}, \boldsymbol{p}; t \mid \{\tilde{\boldsymbol{r}}_{i_a}, \tilde{\boldsymbol{p}}_{i_a}\}_{i_a}^{N_a})$, where $\{\tilde{\boldsymbol{r}}_{i_a}, \tilde{\boldsymbol{p}}_{i_a}\}_{i_a}^{N_a} = \tilde{\boldsymbol{r}}_1, \tilde{\boldsymbol{p}}_1 \ldots \tilde{\boldsymbol{r}}_{N_a}, \tilde{\boldsymbol{p}}_{N_a}$ is a shorthand for the collection of every particle phase-space coordinate. Some method for condensing every individual particle into a more manageable number of parameters is needed.

---

[*]Even though $\boldsymbol{p}$ formally is the phase-space coordinate, not $\boldsymbol{v}$, the latter can in principle be treated as one, since they are directly related via $\boldsymbol{v} = \boldsymbol{p}/(\gamma m_a)$, which is independent of the state of the system.

2.1.1 Ensemble averages

In order to simplify the $6N_a$ variables in (2.8), we make use of the concept of *ensemble averaging*. In principle, we are solving a system of partial differential equations (PDEs), which requires the initial conditions for $6N$ variables, three for every $\tilde{\boldsymbol{r}}_{i_a}(t{=}0)$ and $\tilde{\boldsymbol{p}}_{i_a}(t{=}0)$, respectively, over every species. The solution for any specific set of initial conditions gives the *microstate* of the system. The *ensemble* in this context is the collection microstates which yield the equivalent *macrostate* of the system. That means choosing a large number of macroscopic system variables (integrated variables) and resolutions for them, and then taking the set of all initial conditions that share the same values for the macroscopic variables, within the margins of the resolution. An example of such integrated variables would be ρ and $\boldsymbol{j}$ (without 'tildes' to denote macroscopic quantities), where a finite spatial resolution gives margins for the exact position of every particle; further examples could be the temperature or pressure in a given volume.

The ensemble average, $\langle\cdot\rangle_{\tilde{\Gamma}}$, of a quantity, $\tilde{\chi}$, is simply the average value of that quantity over every microstate in the ensemble:

$$\chi = \langle\tilde{\chi}\rangle_{\tilde{\Gamma}} = \left\langle\tilde{\chi}(\{\tilde{\boldsymbol{r}}_i,\tilde{\boldsymbol{p}}_i\}_i^N)\right\rangle_{\tilde{\Gamma}} = \frac{\int\{\mathrm{d}^3\tilde{r}_i\mathrm{d}^3\tilde{p}_i\}_i^N\,\tilde{\chi}(\{\tilde{\boldsymbol{r}}_i,\tilde{\boldsymbol{p}}_i\}_i^N)\tilde{\Gamma}(\{\tilde{\boldsymbol{r}}_i,\tilde{\boldsymbol{p}}_i\}_i^N)}{\int\{\mathrm{d}^3\tilde{r}_i\mathrm{d}^3\tilde{p}_i\}_i^N\,\tilde{\Gamma}(\{\tilde{\boldsymbol{r}}_i,\tilde{\boldsymbol{p}}_i\}_i^N)} \tag{2.11}$$

where $\tilde{\Gamma}(\{\tilde{\boldsymbol{r}}_i,\tilde{\boldsymbol{p}}_i\}_i^N)$ is the density of the microstate $\{\tilde{\boldsymbol{r}}_i,\tilde{\boldsymbol{p}}_i\}_i^N$ in the ensemble (the index i is now running over *all* N particles in the system, from every species). The word *density* in this context is akin to the use of ditto in the *probability-density function* of a continuous stochastic variable: In a sense, $\tilde{\Gamma}(\{\tilde{\boldsymbol{r}}_i,\tilde{\boldsymbol{p}}_i\}_i^N)$ can be thought of as the (scaled) probability density of a random microstate $\{\tilde{\boldsymbol{r}}_i,\tilde{\boldsymbol{p}}_i\}_i^N$ actually being included in the ensemble.

2.1.2 The distribution function and the Vlasov equation

One of the most important ensemble averages is the ensemble average of the Klimontovich distribution function,

$$\left\langle\tilde{f}_a(\boldsymbol{r},\boldsymbol{p};t\,|\,\{\tilde{\boldsymbol{r}}_{i_a},\tilde{\boldsymbol{p}}_{i_a}\}_{i_a}^{N_a})\right\rangle_{\tilde{\Gamma}} = \left\langle\tilde{f}_a\right\rangle_{\tilde{\Gamma}}(\boldsymbol{r},\boldsymbol{p};t) \equiv f_a(\boldsymbol{r},\boldsymbol{p};t), \tag{2.12}$$

known as the one-particle distribution function – or simply, *the distribution function*. Instead of retaining information of every single particle, f_a now represents the average phase-space density of particles – *this* is the important idea to have in mind concerning distribution functions – which also makes f_a smooth. The average system will have $f_a(\boldsymbol{r},\boldsymbol{p};t)\mathrm{d}^3r\mathrm{d}^3p$ number of particles of species a in the phase-space volume $\mathrm{d}^3r\mathrm{d}^3p$ around the phase-space coordinate $(\boldsymbol{r},\boldsymbol{p})$ at time t. In practice, owing to the large number of particles in any physically relevant system, for some finite resolution Δ^3r and Δ^3p, $f_a(\boldsymbol{r},\boldsymbol{p};t)\Delta^3r\Delta^3p$ will be a very good representation of the actual number of particles in any specific system. Therefore, while the information of every single particle is lost, full information about f_a for all a is, almost by definition, sufficient to fully describe the entire macrostate of the system.

The governing equation for the evolution of the system, may be expressed in terms of the one-particle distribution function, by applying the ensemble average on (2.8):

$$0 = \left\langle \frac{\partial \tilde{f}_a}{\partial t} + \boldsymbol{v} \cdot \frac{\partial \tilde{f}_a}{\partial \boldsymbol{r}} + Z_a^* \tilde{\boldsymbol{K}} \cdot \frac{\partial \tilde{f}_a}{\partial \boldsymbol{p}} \right\rangle_{\tilde{\Gamma}} = \frac{\partial f_a}{\partial t} + \boldsymbol{v} \cdot \frac{\partial f_a}{\partial \boldsymbol{r}} + Z_a^* \left\langle \tilde{\boldsymbol{K}}_a \cdot \frac{\partial \tilde{f}_a}{\partial \boldsymbol{p}} \right\rangle_{\tilde{\Gamma}}. \quad (2.13)$$

The first two terms on the right-hand side of the equation stem from the definition of f_a and the fact that $\boldsymbol{r}$, $\boldsymbol{v}$ and t, as phase-space coordinates, are independent of the microstate $\{\tilde{\boldsymbol{r}}_i, \tilde{\boldsymbol{p}}_i\}_i^N$ of the system. It is therefore possible to lift the scalar product with $\boldsymbol{v}$ outside the ensemble average and reverse the order of averaging and differentiation.

Note, however, that $\tilde{\boldsymbol{K}}$ must be retained inside the average, since it depends on the electric and magnetic fields, which are clearly dependent on the state of the system. Furthermore, the electromagnetic fields are also dependent on the contribution from all the species in the system. We may therefore write

$$\left\langle \tilde{\boldsymbol{K}} \cdot \frac{\partial \tilde{f}_a}{\partial \boldsymbol{p}} \right\rangle_{\tilde{\Gamma}} = \left\langle \tilde{\boldsymbol{K}} \right\rangle_{\tilde{\Gamma}} \cdot \frac{\partial f_a}{\partial \boldsymbol{p}} - \sum_b \tilde{C}_{ab} = \boldsymbol{K} \cdot \frac{\partial f_a}{\partial \boldsymbol{p}} - \sum_b \tilde{C}_{ab}, \quad (2.14)$$

where $\boldsymbol{K} = \left\langle \tilde{\boldsymbol{K}} \right\rangle_{\tilde{\Gamma}}$, and $\tilde{C}_{ab}$ has been introduced to represent the effect on f_a through interactions on the microscopic level, with every other species b (including with a itself)[†]. What this means is that, while the exact microstate of the system may have been sidestepped through f_a, and complete knowledge of the macrostate is given by f_a, the exact evolution of f_a is still affected by the interactions on the microstate level. In other words, $\tilde{C}_{ab}$ represents the effect on the macrostate from the interactions between individual particles, i.e. inter-particle *collisions* – see §2.2 for more on that.

The next step is to disentangle $\boldsymbol{K} = e \left\langle \tilde{\boldsymbol{E}} + \boldsymbol{v} \times \tilde{\boldsymbol{B}} \right\rangle_{\tilde{\Gamma}} = e(\boldsymbol{E} + \boldsymbol{v} \times \boldsymbol{B})$, where $\boldsymbol{E} = \left\langle \tilde{\boldsymbol{E}} \right\rangle_{\tilde{\Gamma}}$ and $\boldsymbol{B} = \left\langle \tilde{\boldsymbol{B}} \right\rangle_{\tilde{\Gamma}}$ are the ensemble-averaged electric and magnetic fields, respectively. Since Maxwell's equations, (2.2), are linear, they may be directly written in ensemble-averaged form,

$$\boldsymbol{\nabla} \cdot \boldsymbol{E} = \frac{\rho}{\epsilon_0}, \quad (2.15\text{a}) \qquad \boldsymbol{\nabla} \times \boldsymbol{E} = -\frac{\partial \boldsymbol{B}}{\partial t}, \quad (2.15\text{c})$$

$$\boldsymbol{\nabla} \cdot \boldsymbol{B} = 0, \quad (2.15\text{b}) \qquad \boldsymbol{\nabla} \times \boldsymbol{B} = \mu_0 \boldsymbol{j} + \mu_0 \epsilon_0 \frac{\partial \boldsymbol{E}}{\partial t}, \quad (2.15\text{d})$$

where

$$\rho = \langle \tilde{\rho} \rangle_{\tilde{\Gamma}} = \sum_a e Z_a^* \int \mathrm{d}^3 p' \; f_a(\boldsymbol{r}, \boldsymbol{p}'; t) = \sum_a \rho_a(\boldsymbol{r}, t), \quad (2.16\text{a})$$

$$\boldsymbol{j} = \left\langle \tilde{\boldsymbol{j}} \right\rangle_{\tilde{\Gamma}} = \sum_a e Z_a^* \int \mathrm{d}^3 p' \; \boldsymbol{v}' f_a(\boldsymbol{r}, \boldsymbol{p}'; t) = \sum_a \boldsymbol{j}_a(\boldsymbol{r}, t), \quad (2.16\text{b})$$

[†]Note that, in principle, this notation fails to include interactions between multiple particles at once; there is a more complete formalism, known as the BBGKY hierarchy (after Bogoljubov, 1960; Born & Green, 1946; Green, 1952; Kirkwood, 1946 and Yvon, 1935), which allows for the treatment of the microscopic interactions of arbitrarily many particles in one single collision.

again, because of the linearity of the momentum integrals. We may now write down (2.13) as

$$\frac{\mathrm{d}f_a}{\mathrm{d}t} = \frac{\partial f_a}{\partial t} + \boldsymbol{v} \cdot \frac{\partial f_a}{\partial \boldsymbol{r}} + eZ_a^*(\boldsymbol{E} + \boldsymbol{v} \times \boldsymbol{B}) \cdot \frac{\partial f_a}{\partial \boldsymbol{p}} = \sum_b \tilde{C}_{ab}, \qquad (2.17)$$

and these equations (2.15, 2.16 & 2.17) represent a closed, self-consistent description of the evolution of the macro-scale system.

To reiterate, the terms on the left-hand side of (2.17) are all expressed in terms of ensemble-averaged quantities, and they represent the system evolution due to collective, macro-scale, plasma interactions. The terms on the right-hand side instead represents the effects of individual particle interactions, i.e. collisions, on the microscopic scale. In some scenarios, e.g. in a sufficiently low-density plasma, where the particles rarely come in close contact with each other, or when the process of interest is much faster than the timescales of collisions, the fields from individual particles may be neglected compared to the macro-fields; in that case, $\tilde{C}_{ab} \to 0$ to a good approximation, and the system is completely governed by the collective behavior of the plasma. In such cases, where the right-hand side vanishes, the plasma is said to be *collisionless* and the governing equation, (2.17) with zero on its right-hand side, is called the *Vlasov (1968) equation*.

2.1.3 Macroscopic quantities obtained from the distribution function

The distribution function can be thought of as containing all the information about the system remaining after ensemble averaging. In order to utilize that information, there must be some way of extracting specific quantities of the system from the distributions. An example of two such macroscopic quantities are the charge and current densities from (2.16). They are extracted from the distribution function by taking *moments* of it.

The most basic moment of the distribution is the particle density in real space,

$$n_a = n_a(\boldsymbol{r}, t) = \int \mathrm{d}^3p' \ f_a(\boldsymbol{r}, \boldsymbol{p}'; t). \qquad (2.18)$$

Other macroscopic quantities can be extracted via moments in a similar fashion. For an arbitrary quantity $\chi = \chi(\boldsymbol{r}, \boldsymbol{p}'; t)$, its macroscopic counterpart is given by

$$\chi_a(\boldsymbol{r}, t) \equiv \langle \chi(\boldsymbol{r}, \boldsymbol{p}'; t) \rangle_a = \frac{1}{n_a} \int \mathrm{d}^3p' \ \chi(\boldsymbol{r}, \boldsymbol{p}'; t) \ f_a(\boldsymbol{r}, \boldsymbol{p}'; t). \qquad (2.19)$$

From this definition, we see that, e.g., $\boldsymbol{j}_a$ from (2.16), can be written in terms of a distribution average as $\boldsymbol{j}_a = eZ_a^* n_a \langle \boldsymbol{v} \rangle_a = eZ_a^* n_a \boldsymbol{v}_a$. In other words, the current density associated with species a is simply the average (or fluid) flow velocity scaled by the charge of a particle of species a, eZ_a^*, and its density, n_a, as one would expect heuristically.

2.2 Collisions

While the Vlasov system of equations, (2.15, 2.16 & 2.17) with $\tilde{C}_{ab} \to 0$, is entirely self-contained and can be integrated as is (with some "minor" complications due to causality considerations which we will not address), we are still lacking an adequate description of the cases where collisions cannot be neglected. Since $\tilde{C}_{ab}$ represents the effect of micro-scale, inter-particle interactions, we still, in principle, require knowledge of the microstate, $\{\tilde{\boldsymbol{r}}_i, \tilde{\boldsymbol{p}}_i\}_i^N$, of the system. Ideally, we would like to have an approximation of $\tilde{C}_{ab}$ that only depends on the macroscopic state. We therefore introduce the *collision operator*, $\hat{C}_{ab} = \hat{C}[f_a, f_b]$, which represents the effect of inter-particle collisions on the evolution of the distribution function. There is now no longer a requirement for knowledge of the microstate of the system – it only depends on f_a and f_b. Depending on the complexity required in the modeling, different collision operators have been devised; naturally, these will result in different levels of accuracy depending on situation and intended usage.

In order to not introduce unnecessary complexity due to relativistic effects, we have here changed to a *non-relativistic* treatment of collisions in this section. This is usually indicated by the use of $\boldsymbol{v}$ as the phase-space coordinate instead of $\boldsymbol{p} \simeq m_a \boldsymbol{v}$ (for $v \ll c$). Appropriate relativistic generalizations are available (Beliaev & Budker, 1956; Braams & Karney, 1987).

2.2.1 Requirements on a collision operator

Since the collision operator is meant to model the effects of the microscopic inter-particle interactions on the macroscopic distribution function, there are limitations on how the operator can be designed. Because the microscopic interactions obey certain conservation properties, so must the overall macroscopic effects.

The first conservation law is that of the number of particles (ignoring collisional ionization and nuclear reactions). The collision cannot change the number of particles. The individual collision is assumed to occur on timescales much shorter than that of any other process in the system, which means that the collision itself only directly changes the momenta of the colliding particles; the position of the colliding particle is only indirectly affected through the change in its velocity. This means that collisions cannot directly affect the density profile of a species, i.e. the rate of change in the density due to collisions must be

$$\frac{\partial n_a}{\partial t}\bigg|_{\text{coll.}} = \sum_b \int \mathrm{d}^3 v' \, \hat{C}[f_a, f_b] = 0, \tag{2.20}$$

at every point in space. Also, since the collisions are assumed not to affect the species of the colliding particles, we may generalize the statement to saying that each integral in the sum must vanish separately, not just the whole sum.

The next conserved macroscopic quantities are momentum and energy. Since we neglect collisions which change the identity of the particles – such as collisional impact ionization – the collisions are all elastic, hence the conservation of (kinetic) energy. However, both momentum and energy can still be transferred between individual particles in a collision, which means that the conservation laws have to

be expressed in terms of the respective rates of momentum and energy transfer between species. For momentum, we have

$$\int \mathrm{d}^3 v' \; \boldsymbol{p}' \hat{C}[f_a, f_b] = - \int \mathrm{d}^3 v' \; \boldsymbol{p}' \hat{C}[f_b, f_a], \tag{2.21}$$

and for energy,

$$\int \mathrm{d}^3 v' \; \frac{m_a v'^2}{2} \hat{C}_{ab} = - \int \mathrm{d}^3 v' \; \frac{m_b v'^2}{2} \hat{C}_{ba} \tag{2.22}$$

for any species a and b. In the special case of inter-species collisions ($b = a$), the integrals of (2.21) and (2.22) must each vanish.

The H-theorem

A final requirement for a physical collision operator is that it should never decrease entropy. While this property does not directly stem from the microscopic nature of collisions – indeed, time reversibility of the microscopic processes dictates that a system should just as well be able to spontaneously decrease its entropy – it is a widely observed phenomenon, codified as the second law of thermodynamics. Boltzmann (1872) introduced a quantity H (which he originally denoted "E" as it was a substitute for entropy) to show that entropy always increases – hence the name "H-theorem". Yet, he proved that under the assumption that every colliding particle is randomly chosen from the distribution of particles, which fundamentally, through the act of ensemble averaging to create the distribution, ignores the time reversibility of the microscopic processes, thus inevitably leading to non-decreasing entropy.

For all practical purposes, however, we may take the increase of entropy as a postulated requirement for a collision operator. While Boltzmann (1872) formulated his quantity H in terms of a distribution in energy, we write it here in terms of the phase-space distribution

$$H_a = H_a(t) = \iint \mathrm{d}^3 r' \, \mathrm{d}^3 v' \; f_a(\boldsymbol{r}', \boldsymbol{v}'; t) \log[f_a(\boldsymbol{r}', \boldsymbol{v}'; t)], \tag{2.23}$$

which only differ from the thermodynamical entropy by a negative constant factor. The rate of change may now be expressed as

$$\frac{\mathrm{d}H_a}{\mathrm{d}t} = \iint \mathrm{d}^3 r' \, \mathrm{d}^3 v' \; \frac{\mathrm{d}f_a}{\mathrm{d}t} \Big[\log(f_a) + 1 \Big]. \tag{2.24}$$

Note that the way collisional effects are introduced in (2.17), $\mathrm{d}f_a/\mathrm{d}t$ may be replaced by $\sum_b \hat{C}_{ab}$. Next, the second term in the brackets vanishes due to conservation of particle number, (2.20), which results in

$$\frac{\mathrm{d}H_a}{\mathrm{d}t} = \sum_b \iint \mathrm{d}^3 r' \, \mathrm{d}^3 v' \; \hat{C}_{ab} \log(f_a). \tag{2.25}$$

The condition on the collision operator, to increase entropy, S, can therefore be written as

$$\frac{\mathrm{d}S}{\mathrm{d}t} \propto - \sum_a \frac{\mathrm{d}H_a}{\mathrm{d}t} \geq 0. \tag{2.26}$$

Note that this condition does not mean that the entropy change has to be positive for every species. Rather, only the net change in entropy for the whole system has to be positive. Indeed, if two species of different temperatures are being thermodynamically equilibrated, then the hotter species will lose entropy, $\Delta H_{\text{hot}} > 0$, and the cooler species will gain entropy, $\Delta H_{\text{cold}} < 0$, while still resulting in a net entropy gain of $\Delta S \propto -(\Delta H_{\text{hot}} + \Delta H_{\text{cold}}) > 0$.

While the formulation of the H-theorem may sound rather abstract and technical, it has a more concrete effect: collisions create a drive towards a specific distribution with maximum entropy. Maxwell (1860) was first to derive this distribution on heuristic ground, followed by Boltzmann (1872), who came to the same conclusions after analyzing the H-theorem. The distribution in question, now known as the *Maxwell–Boltzmann distribution*, is

$$f_a^{(\text{MB})}(\boldsymbol{r}, \boldsymbol{v}; t) = \frac{n_a}{(2\pi T_a/m_a)^{d/2}} \exp\left(-\frac{m_a v^2}{2 T_a}\right), \qquad (2.27)$$

in d dimensions, for a population with density n_a and temperature T_a. This distribution is formulated for a non-relativistic population, where the kinetic energy, $m_a v^2/2$, of the particles is much smaller than their rest energy, $m_a c^2$. For relativistic particles, the distribution can be generalized to the *Maxwell–Jüttner distribution* after Jüttner (1911); in terms of a momentum distribution, it is given as

$$f_a^{(\text{MJ})}(\boldsymbol{r}, \boldsymbol{p}; t) = \frac{n_a}{4\pi (m_a c)^3 \Theta_a K_2(1/\Theta_a)} \exp\left(-\frac{\gamma}{\Theta_a}\right), \qquad (2.28)$$

where $\Theta_a = T_a/m_a c^2$, K_2 is the (second-order) modified Bessel function of the second kind, and $\gamma = \gamma(p)$ is the Lorentz factor.

2.2.2 The Fokker–Planck collision operator

While a vast number of operators, all with their own assumptions, have been used to analyze the effects of collisions, one of the most commonly used operators is the *Fokker–Planck operator*. It is based on the *Coulomb interaction* between charged particles. Unlike the hard-sphere, close collisions that Maxwell (1860) and Boltzmann (1872) considered, which result in large angle scattering, the long range of the Coulomb force results in the prevalence of small-angle, grazing collisions, where the momenta of the colliding particles are only slightly changed. Therefore, the collision operator, which acts on the distribution function, should only directly affect the *momentum space* portion of the distribution.

In fact, the small-angle nudges in the momenta of the particles can be viewed as a random walk in momentum space. When considering the large number of particles encompassed by the distribution function, heuristically, this random walk should result in some form of diffusion of the distribution function in momentum space. Indeed, we may write a general form of the collision operator consisting of a *diffusion* term, D_{kl}, and an *advection/friction/drift* term, A_k. The advection term is added to account for such effects as friction when a particle is moving relative to the background – intuitively, we would expect a fast-moving population of particles
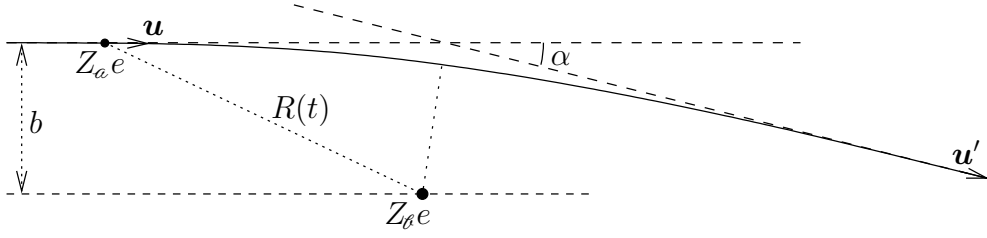
Figure 2.1: Illustration of a Coulomb collision between a particle of species a and b, in the rest frame of particle b. The collision has an impact parameter b and results in a change in the trajectory of particle a by an angle α.

to slow down due to collisions with the background, not only diffuse. In general, an advection–diffusion equation can be written on the form

$$\frac{\mathrm{d}f}{\mathrm{d}t} = \frac{\partial}{\partial v_k}\left[A_k f + \frac{\partial}{\partial v_l}\left(D_{kl}f\right)\right] = \hat{C}[f], \tag{2.29}$$

where tensor-index notation has been adapted (e.g. $v_k \doteq \boldsymbol{v}$, and like indices are summed, such that $\partial/\partial v_k\,[A_k f] = \partial/\partial \boldsymbol{v} \cdot [\boldsymbol{A}f]$). These terms can then be further divided into the contributions from the different species a and b: A_k^{ab} and D_{kl}^{ab}.

Coulomb collisions

The starting point for the Fokker–Planck operator is the electrostatic interaction between two particles via the Coulomb force $Z_a Z_b e^2/(4\pi\epsilon_0 R^2)$, where R is the distance between the particle a and b. By limiting ourselves to binary collisions, we may utilize the existing framework for two-body mechanics: we shift to the rest frame of particle b and use the relative velocity $\boldsymbol{u} = \boldsymbol{v}_a - \boldsymbol{v}_b$; we view b as stationary and use the reduced mass $m_{ab} = m_a m_b/(m_a + m_b)$ for particle a. The resulting interaction is illustrated in Fig. 2.1, where the collision results in a deviation by an angle α to the trajectory of particle a.

If indeed $\alpha \ll 1$, then R can be approximated as $R = R(t) \approx [b^2 + (ut)^2]^{1/2}$, and the change in velocity, $\Delta\boldsymbol{u}$, lies (almost) exclusively in the vertical direction of Fig. 2.1. The magnitude of the change is given by the impulse due to the Coulomb force

$$m_{ab}\Delta u \approx \int_{-\infty}^{\infty} \frac{Z_a Z_b e^2}{4\pi\epsilon_0 R^2(t)}\,\frac{b}{R(t)}\,\mathrm{d}t = \frac{Z_a Z_b e^2}{4\pi\epsilon_0}\int_{-\infty}^{\infty}\frac{b}{[b^2 + (ut)^2]^{3/2}}\,\mathrm{d}t = \frac{Z_a Z_b e^2}{2\pi\epsilon_0 bu}, \tag{2.30}$$

which gives a scattering angle

$$\alpha \approx \frac{\Delta u}{u} \approx \frac{Z_a Z_b e^2}{2\pi\epsilon_0 b m_{ab} u^2}. \tag{2.31}$$

The *deflection* of the velocity, i.e. the change in the direction perpendicular to the initial trajectory, is

$$\Delta u_\perp = u\sin\alpha \approx u\,\frac{Z_a Z_b e^2}{2\pi\epsilon_0 b m_{ab} u^2} = \frac{Z_a Z_b e^2}{2\pi\epsilon_0 m_{ab}}\,\frac{1}{bu}, \tag{2.32}$$

and the corresponding *slowing-down* component, i.e. change in the direction parallel to the initial trajectory, is

$$\Delta u_\parallel = u\left(\cos\alpha - 1\right) \approx -\frac{u}{2}\left(\frac{Z_a Z_b e^2}{2\pi\epsilon_0 b m_{ab} u^2}\right)^2 = -\left(\frac{Z_a Z_b e^2}{2\pi\epsilon_0 m_{ab}}\right)^2 \frac{1}{2b^2 u^3}. \tag{2.33}$$

Note that, although Fig. 2.1 illustrates the interaction of two mutually attracted particles, i.e. oppositely charged particles, the mathematical framework holds also for particles with the same charge.

An interesting observation here is that the scattering angle α and therefore the changes to the velocity, depend on the relative velocity of the particles, u. A larger velocity results in a smaller scattering angle; heuristically, this can be explained by the shortened time the particles have to interact if their relative velocity is high. Furthermore, the slowing-down component is much more sensitive, $\Delta u_\parallel \propto u^{-3}$, than the deflection component, $\Delta u_\perp \propto u^{-1}$. Importantly, a similar behavior is carried over to the advection and diffusion terms in the Fokker–Planck operator.

Another important concept in conjunction with collisional effects is the *collision frequency* – often denoted with the symbol ν. It is loosely defined as the rate at which collisions cause a significant change to the velocity of the particle, e.g. a $\sim 90°$ deviation in trajectory or a order-unity change in the speed of the particle. Often, the *collisionality* of a plasma is measured by comparing the various collision frequencies to the timescales of other mechanisms affecting the plasma. Linked to the collision frequency, one can also talk about the collisional *mean free path*, which gives a length scale, over which collisional effects become important.

From one collision to the statistics of many

In order to construct the Fokker–Planck collision operator, we need to treat the Coulomb interactions statistically, and compute the probability for all possible scattering outcomes of every part of f_a, in the possible interaction with every part of f_b. That presents a problem, since the Coulomb interaction is long range – note for instance that $\alpha \propto b^{-1}$. Without any way of "cutting off" the range of the Coulomb force, the contribution from all the different parts of the plasma would make the collision operator divergent. Fortunately, thanks to the phenomenon known as *Debye shielding*, the range of the electrostatic potential (and hence the electric field) is suppressed by a factor $\exp(-R/\lambda_D)$, where $\lambda_D = [\epsilon_0 T_e/(n_e e^2)]^{1/2}$ is called the *Debye length*. The suppression of the electric field at distances $\gtrsim \lambda_D$ effectively gives a lower bound on the scattering angle and avoids the divergence in the collision operator.

Without going into any further details – for a thorough derivation, the reader is referred to a textbook on collisions in plasmas, for instance the book by Helander & Sigmar (2002) – the Fokker–Planck operator can be expressed in terms of the so called *Rosenbluth potentials* (Rosenbluth, MacDonald & Judd, 1957)

$$\begin{aligned}
\varphi_b(\boldsymbol{v}) &= -\frac{1}{4\pi}\int \frac{f_b(\boldsymbol{v}')}{|\boldsymbol{v}-\boldsymbol{v}'|}\,\mathrm{d}^3 v', \\
\psi_b(\boldsymbol{v}) &= -\frac{1}{8\pi}\int |\boldsymbol{v}-\boldsymbol{v}'|\,f_b(\boldsymbol{v}')\,\mathrm{d}^3 v',
\end{aligned} \tag{2.34}$$

for collisions with species b. The advection and diffusion parameters are then given by

$$
\begin{aligned}
A_k^{ab} &= \left(1 + \frac{m_a}{m_b}\right) \frac{Z_a Z_b e^2 \log \Lambda}{\epsilon_0 m_a} \frac{\partial \varphi_b}{\partial v_k}, \\
D_{kl}^{ab} &= -\frac{Z_a Z_b e^2 \log \Lambda}{\epsilon_0 m_a} \frac{\partial^2 \psi_b}{\partial v_l \partial v_k},
\end{aligned}
\tag{2.35a}
$$

and the Fokker–Planck operator for species a colliding with species b becomes

$$
\hat{C}[f_a, f_b] = \frac{\partial}{\partial v_k}\left[A_k^{ab} f_a + \frac{\partial}{\partial v_l}\left(D_{kl}^{ab} f_a\right)\right].
\tag{2.35b}
$$

The *Coulomb logarithm*, $\log \Lambda$, included in the expressions for A_k^{ab} and D_{kl}^{ab} is a consequence of the $\sim R^{-1}$ dependence of the Coulomb potential, and it arises due to an integration over all scattering angles, α, or equivalently all impact parameters, b,

$$
\log \Lambda \sim \int \frac{\mathrm{d}(\sin \alpha)}{\sin \alpha} \sim \int \frac{\mathrm{d}b}{b} \sim \log\left(\frac{b_{\max}}{b_{\min}}\right).
\tag{2.36}
$$

The upper limit, $b_{\max} \sim \lambda_{\mathrm{D}}$, in the impact-parameter integral stems from Debye shielding, and it corresponds to a lower limit on the scattering angle $\alpha_{\min}$. However, the details of the lower limit $b_{\min}$ are more complicated. One approach is to take $b_{\min} = \max\{\lambda_{\mathrm{B}}, b_\perp\}$, where $\lambda_{\mathrm{B}} = \hbar/p_a$ is the de Broglie wavelength and $b_\perp = Z_a Z_b e^2/(4\pi\epsilon_0 m_{ab} u^2)$ is called the impact parameter of closest approach; this approach is commonly used in implementations of collisions in particle-in-cell codes (§ 2.4), although this prescription has also been criticized (Mulser, Alber & Murakami, 2014).

It is crucial for the derivation of the Fokker–Planck operator that $\log \Lambda \gg 1$, because otherwise, the individual collisions cannot be assumed to all have a small scattering angle. In fusion plasmas $\log \Lambda \sim 10-20$, so there the Fokker–Planck operator gives a good representation of the effects of collisions for most parts. However, in laser-plasmas $\log \Lambda \sim 2-7$, which means that there is a significant probability of large-angle collisions, which is a problem for the Fokker–Planck operator; in simulation algorithms treating collisions in laser-plasmas, the smallness of the Coulomb logarithm is usually handled by imposing a lower limit $\log \Lambda \geq 2$ and then modifying the collision statistics in various ways (Sentoku & Kemp, 2008; Pérez *et al.*, 2012).

2.3 Continuum Vlasov–Maxwell solvers

While kinetic theory immensely simplifies the modeling of a plasma, compared to the impossibly large task of solving the equations of motion for every particle, the set of kinetic equations is still a coupled set of PDEs, which require numerical tools to solve, except in a very limited set of highly idealized cases. One way is to take equations (2.15, 2.16 & 2.17), discretize them in time and onto an *Eulerian*[‡] simulation grid in phase space, and then use PDE-solving methods to find a solution for

---

[‡]The denomination "Eulerian" stems from the two flow specifications of a fluid, *Eulerian* and *Lagrangian*, where the fluid flow field is either specified on a fixed coordinate system or along the trajectories of "packets" of fluid, respectively. In the case of a continuum Vlasov–Maxwell solver, the "fluid" in question is the phase-space distribution.

$f_a(\boldsymbol{r}, \boldsymbol{v}; t)$. These methods are called *continuum* or *Vlasov–Maxwell/kinetic solvers*, because they solve the Vlasov/kinetic equation coupled with Maxwell's equations in a continuum framework.

On the other hand, the fact that the full phase space is discretized is also one of the main difficulties of the continuum methods. Since phase space has a minimum of twice the number of dimensions (both $\boldsymbol{r}$ and $\boldsymbol{p}$) as the configuration space modeled, that means that we may have to simulate up to six dimensions, plus time. In addition, not all areas of phase space are of the same physical relevance, e.g. some areas might be devoid of particles or have a very low phase space density; yet, these less important areas are still part of the computation. The computational cost can therefore grow prohibitively fast for simulation of more than one or two spatial dimensions.

Another complication that might arise due to the complexity of Vlasov–Maxwell methods is that of code development. As we have seen in §2.2.2, a rather simple physical phenomenon, such as the slight deviation of the particle trajectory due to their Coulomb interaction, may require rather complex expressions in terms of their effect on the evolution of the distribution function. Effectively incorporating new features into a Vlasov–Maxwell code may therefore be rather challenging.

However, for applications which require a fully kinetic description and can be simulated with one or two spatial dimensions, or only require a rather low resolution, continuum solvers are a powerful tool. A selection of such applications are electrostatic shocks (Svedung Wettervik, DuBois & Fülöp, 2016; Pusztai *et al.*, 2018; Sundström *et al.*, 2019), which will be examined further in this thesis, kinetic plasma instabilities (Cagas *et al.*, 2017; Skoutnev *et al.*, 2019), and kinetic effects in magnetic dynamos (Rincon *et al.*, 2016§; Pusztai *et al.*, 2020). Furthermore, Vlasov–Maxwell solvers may also be used as a reference; thanks to their low noise and possibly high fidelity, their output from a standardized problem could be used as a benchmark for other types of simulation codes, such as fluid or particle-in-cell codes.

Additional reading on these types of simulation frameworks can be found in the book by Shoucri (2011), or in the (very extensive) PhD thesis by Juno (2020).

Gkeyll

During the course of the work included in this thesis, one of the tools that were used is `Gkeyll`¶ (Juno *et al.*, 2018). `Gkeyll` is a versatile tool containing Eulerian solvers for the (non-relativistic) Vlasov–Maxwell equations as well as for gyro-kinetic equations and various sets of multi-fluid equations. The Vlasov–Maxwell system, which we are most interested in, is discretized in phase space with a discontinuous Galerkin finite element method, and discretized in time with a strong stability-preserving Runge–Kutta method, which gives fully explicit time stepping. The discontinuous Galerkin method benefits from both the power of finite element methods, such as high-order accuracy and the ability to handle complicated geometries, as well as

---

§Although Rincon *et al.* (2016) used a Vlasov–Maxwell method, they reduced the computational cost by treating the electrons with a fluid model.

¶Code documentation can be found at: https://gkyl.readthedocs.io/en/latest/.

from the advantages of finite volume methods, such as the introduction of limiters to ensure the positivity of the distribution function to enforce stability and physicality of the solution.

Beyond the collisionless Vlasov–Maxwell system, `Gkeyll` also supports effects of collisions with either the BGK operator (Bhatnagar, Gross & Krook, 1954) or the Dougherty (1964) (Dougherty & Watson, 1967) operator – the latter is sometimes also referred to as a Lenard–Bernsein (1958) operator. While these operators satisfy the physical requirements in § 2.2.1, they are not as advanced and lack the complex velocity dependence found in the Fokker–Planck operator, which means that their scope of application is limited to near-thermal distributions. A detailed account of the implementation of the collisions in `Gkeyll` can be found in the recent paper by Hakim *et al.* (2020).

2.4 Particle-in-cell methods

A more popular framework to simulate kinetic plasmas is the particle-in-cell (PIC) technique (Pukhov, 2016). This method goes back to the basic idea to compute the trajectories of individual particles, although with much fewer computational *macroparticles*. Instead of the relatively complicated system of non-linear PDEs that is used in kinetic theory, PIC methods integrate the equations of motion for the finite number of macroparticles, (2.1), albeit with every macroparticle weighted to represent a large number of "real" *microparticles*, i.e. q_a and m_a are scaled up by a factor, while keeping the charge-to-mass ratio q_a/m_a constant. The macroparticles usually also have a finite spatial extent – their *shape function* – which reduces discretization noise. When the Lorentz force on the macroparticle is computed, the (discretized) field is interpolated together with the shape function; for more detail, see for instance the appendix of Derouillat *et al.* (2018). By its nature, the PIC solver can be viewed as a finite element solver of the Vlasov–Maxwell system using the *Lagrangian* (phase-space) flow specification – as opposed to Eulerian continuum solvers, where the (phase-space) flow is computed on a fixed grid.

Maxwell's equations, (2.2), are solved on a grid of computational "cells". The charge and current densities, (2.3), are projected onto a staggered grid via the particle shape functions. The weighting and shape of the macro particles allows the field–plasma interaction to emulate that of the simulated system – thanks to the scaled charge and current densities, the particle-field interaction dynamics is kept unchanged. The PIC procedure thus consists of two operations: (*i*) given the position and velocity/momentum of all particles, calculate the fields; (*ii*) given the fields and previous velocity of the particle, calculate the new position and velocity/momentum of the particle – commonly referred to as the *particle pusher*. These two operations are iterated back and forth for every simulated time step, and constitute the essence of a PIC code. In order to increase the numerical stability, more complex strategies are employed, such as the, de facto standard, "Boris (1970) pusher".

The PIC method benefits from its conceptually simple algorithm. By relying on computing the trajectories of macroparticles, the method can aid the understanding of a physical problem by allowing particles to be followed through phase space – which would otherwise be challenging to do in a continuum framework. Furthermore,

since every particle push occurs independently between the field calculations, PIC codes are naturally well-adapted for massively parallelized computation.

The main computational bottleneck for PIC simulations, however, is usually the number of macro particles in the simulation. Since PIC codes do not have to include momentum space in their computational grid, they are not as affected by higher dimensions as Vlasov–Maxwell solvers can be. One way of viewing PIC codes is that they solve for a random statistical sampling of the initial distribution function in all its dimensions, thus breaking the "curse of dimensionality" with a limited number of statistical samples – the macroparticles. However, the limited number of macroparticles also usually results in rather noisy results due to a relatively coarse-grained projection of the particles onto the charge and current density grid. Unfortunately, due to the statistical nature of PIC simulations, the noise level only decreases as $\sim \bar{N}^{-1/2}$ with the number of macroparticles, $\bar{N}$.

The field–particle interaction is limited by the finite grid resolution of the fields, meaning that microscopic particle interactions mediated by the field – such as collisions – are similarly limited by the computational grid resolution. Due to computational constraints, the grid resolution is much too coarse to accurately capture collisional effects. Instead, Monte Carlo schemes are being used to emulate the "random kicks" the (micro) particles experience due to collisions. These schemes operate by calculating the probability distribution for a certain angular deviation to the particle momentum due to collisions during one simulation time step. The most common method is to implement a scheme with binary collisions between macroparticles (Sentoku & Kemp, 2008; Nanbu, 1997; Nanbu & Yonemura, 1998; Pérez *et al.*, 2012), which are mutually scattered according to the scattering probability distribution, such that momentum and energy are being conserved – at least statistically.

The relatively simple basic principle of operation of PIC codes also means that there are a wide variety of different PIC codes available to use more or less freely – PIC codes are much more common than Vlasov–Maxwell codes. Together with the fact that PIC codes can readily handle relativistic particle motion, it is no surprise that the vast majority of laser-plasma simulations are done with PIC codes. As with binary collisions, PIC methods can more easily be adapted to emulate quantum mechanical effects on the macroparticles, such as interactions with photons (e.g. emission/absorption and quantum-electrodynamical effects) or ionization, all of which are highly non-trivial to implement in a continuum framework and may be of great importance to laser–plasma interactions. An even remotely extensive account of studies performed with PIC codes would be prohibitively long; in fact, PIC simulations have become so ubiquitous that nowadays they accompany almost all experimental findings (Faure *et al.*, 2004; Haberberger *et al.*, 2012; Higginson *et al.*, 2018; Fiuza *et al.*, 2020).

Smilei

In cases which have required the functionalities of a PIC code, the tool used here has been Smilei[∥] (Derouillat *et al.*, 2018). It is co-developed by high-performance-

---

[∥]Code documentation can be found at: https://smileipic.github.io/Smilei/.

computing specialists and physicists, in order to be as modular as possible and perform efficiently on large-scale supercomputers. Smilei is complemented by a large set of run-time diagnostics (based on the HDF5 file format) and user-friendly (Python) post-processing tools complements the code. The modularity of Smilei gives it access to various additional physics modules, among which are field ionization, binary collisions and collisional impact ionization – all of which with high relevance to the work included in this thesis.

Chapter 3

Laser–plasma interactions

The interaction between the electric and magnetic fields of laser light with a plasma may in many cases be exceedingly complex, and governed by highly non-linear physics, almost exclusively amenable to numerical computations. However, there are some basic guiding principles which aid the understanding of various phenomena observed in laser-plasmas. In this chapter, we will review some of the fundamentals of laser–plasma interactions, and give special attention to laser-based plasma heating.

After that, we will discuss the contributions made by the included papers in this thesis. We will start by discussing laser-based isochoric heating and the simulation work on inverse bremsstrahlung heating done in paper **B**. Then we discuss the effects of collisions on the electrostatic shock waves from the simulations in paper **C**; we also discuss the impact of the simulation algorithm used for the collisional effects, with respect to the differing results in paper **C** from that of Turrell, Sherlock & Rose (2015). Lastly, we discuss a semi-analytical model for the effects of a weak collisionality on electrostatic shocks, developed in paper **A**.

3.1 Review of some of the basics concepts of laser–matter interactions

With the advent of laser technology, came the opportunity of using and studying highly coherent and monochromatic light, which is modeled by a plane wave, usually with some modulation superimposed. In this section, we will review the basic concepts of electromagnetism that lead to the propagation of waves in § 3.1.1, followed in § 3.1.2 by single-particle dynamics in a plane wave field, and finally § 3.1.3 we will consider the plasma dynamics when irradiated by laser light.

3.1.1 Electromagnetism

In this section, we will give a brief overview of concepts from electromagnetism such as the scalar and vector potentials, plane waves and how they affect the motion of charged particles. More detailed treatments of these concepts can be found in textbooks on electrodynamics, such as the one by Jackson (1999), and more spe-

cialized textbooks on laser–plasma interactions, such as the ones by Gibbon (2005) and Macchi (2013).

While the differential form of Maxwell's equations (2.15) is one possibility to describe the evolution of the electromagnetic fields, there are other formulations. Alternatively, the electromagnetic dynamics may be described with a formalism based on the vector and scalar potentials $\boldsymbol{A}$ and ϕ, respectively, where

$$\boldsymbol{B} = \boldsymbol{\nabla} \times \boldsymbol{A} \quad \text{and} \quad \boldsymbol{E} = -\frac{\partial \boldsymbol{A}}{\partial t} - \boldsymbol{\nabla}\phi. \tag{3.1}$$

These expressions with potentials are possible due to the zero divergence of the magnetic field (2.15b), and Faraday's law (2.15c),

$$0 = \boldsymbol{\nabla} \times \boldsymbol{E} + \frac{\partial \boldsymbol{B}}{\partial t} = \boldsymbol{\nabla} \times \left(\boldsymbol{E} + \frac{\partial \boldsymbol{A}}{\partial t}\right). \tag{3.2}$$

Furthermore, since the potential forms of the fields (3.1) guarantee that these two of Maxwell's equations are satisfied, the full field dynamics can then be expressed with the remaining two equations, Gauss's (2.15a) and Ampère's (2.15d) laws, rewritten using the potential formalism:

$$-\nabla^2\phi - \frac{\partial}{\partial t}\left[\boldsymbol{\nabla} \cdot \boldsymbol{A}\right] = \rho/\epsilon_0, \tag{3.3a}$$

$$-\nabla^2\boldsymbol{A} + \frac{1}{c^2}\frac{\partial^2 \boldsymbol{A}}{\partial t^2} + \boldsymbol{\nabla}\left(\boldsymbol{\nabla} \cdot \boldsymbol{A} + \frac{1}{c^2}\frac{\partial \phi}{\partial t}\right) = \mu_0\boldsymbol{j}, \tag{3.3b}$$

where the speed of light $c = (\epsilon_0\mu_0)^{-1/2}$ now explicitly appears.

One advantage of the potential formalism is in the freedom to choose the gauge of the potentials without affecting the physical fields, i.e. the transformation

$$\boldsymbol{A} \to \boldsymbol{A} + \boldsymbol{\nabla}\vartheta \quad \text{and} \quad \phi \to \phi - \frac{\partial \vartheta}{\partial t}, \tag{3.4}$$

for any function $\vartheta = \vartheta(\boldsymbol{r}, t)$. This allows us to choose, for instance, the Lorenz (1867) gauge

$$\boldsymbol{\nabla} \cdot \boldsymbol{A} + \frac{1}{c^2}\frac{\partial \phi}{\partial t} = 0, \tag{3.5}$$

which transforms (3.3) into two independent wave equations:

$$\nabla^2\phi - \frac{1}{c^2}\frac{\partial^2 \phi}{\partial t^2} = -\rho/\epsilon_0, \tag{3.6a}$$

$$\nabla^2\boldsymbol{A} - \frac{1}{c^2}\frac{\partial^2 \boldsymbol{A}}{\partial t^2} = -\mu_0\boldsymbol{j}. \tag{3.6b}$$

Plane waves

One of the most important consequences of Maxwell's equations is that they allow for wave solutions. In vacuum, i.e. $\rho = 0$ and $\boldsymbol{j} = 0$, (3.6) become two independent homogeneous wave equations that permit *plane wave* solutions, which are harmonically oscillating in both time and space. We may make use of the harmonic nature

of the plane wave by expressing the temporal and spatial dependence using the complex exponential, $\exp[\mathrm{i}(\boldsymbol{k} \cdot \boldsymbol{r} - \omega t)]$, where i is the imaginary unit, ω is the angular frequency of the harmonic oscillation, $\boldsymbol{k} = k\hat{\boldsymbol{k}}$ is the *wave vector* and $\hat{\boldsymbol{k}}$ is the unit vector pointing in the direction of wave propagation. Physical (real) quantities are, by convention, taken as the real parts of their complex counterparts.

With the introduction of the complex harmonic time dependence, time and spatial derivatives are now transformed to multiplications by $\mathrm{i}\omega$ and $\mathrm{i}\boldsymbol{k}$, respectively. The wave equation for the vector potential (3.6b), then becomes

$$k^2 \boldsymbol{A} - \frac{\omega^2}{c^2} \boldsymbol{A} = 0, \tag{3.7}$$

which, a posteriori, is satisfied by

$$\boldsymbol{A} = -\mathrm{i}A_0 \hat{\boldsymbol{e}} \exp[\mathrm{i}(\boldsymbol{k} \cdot \boldsymbol{r} - \omega t)], \tag{3.8}$$

where A_0 is the amplitude of the oscillation, $\hat{\boldsymbol{e}}$ is a constant unit vector describing the polarization of the wave, and k and ω must satisfy $\omega/k = c$, giving the speed of wave propagation; the factor $-\mathrm{i}$ is just an arbitrary phase factor. We may further specify the gauge such that the polarization of the vector potential satisfies $\hat{\boldsymbol{e}} \cdot \boldsymbol{k} = 0$, i.e. perpendicular to the direction of propagation, which also gives $\boldsymbol{\nabla} \cdot \boldsymbol{A} = 0$. By the Lorenz condition (3.5) and the wave equation (3.6a), ϕ must now be a constant in both time and space; we may thus choose $\phi \equiv 0$. The electric and magnetic fields of the plane wave can then be expressed as

$$
\begin{aligned}
\boldsymbol{E} &= -\frac{\partial \boldsymbol{A}}{\partial t} = \mathrm{i}\omega \boldsymbol{A} = \omega A_0 \hat{\boldsymbol{e}} \exp[\mathrm{i}(\boldsymbol{k} \cdot \boldsymbol{r} - \omega t)], \\
\boldsymbol{B} &= \boldsymbol{\nabla} \times \boldsymbol{A} = \mathrm{i}\boldsymbol{k} \times \boldsymbol{A} = k A_0 \, \hat{\boldsymbol{k}} \times \hat{\boldsymbol{e}} \, \exp[\mathrm{i}(\boldsymbol{k} \cdot \boldsymbol{r} - \omega t)] = \frac{1}{c}\hat{\boldsymbol{k}} \times \boldsymbol{E}.
\end{aligned}
\tag{3.9}
$$

From the last equality, we see that $\boldsymbol{B}$ is perpendicular to both $\boldsymbol{E}$ and $\boldsymbol{k}$.

The polarization, $\hat{\boldsymbol{e}}$, is perpendicular to the direction of propagation, $\hat{\boldsymbol{k}}$, but may otherwise be chosen without constraints. For simplicity, we may choose our coordinate system such that $\hat{\boldsymbol{k}} = \hat{\boldsymbol{x}}$. Then the wave equation allows us to choose two linearly independent basis vectors for the polarization, e.g. the remaining Cartesian unit vectors $\hat{\boldsymbol{y}}$ and $\hat{\boldsymbol{z}}$. For instance, $\hat{\boldsymbol{e}}$ may be chosen as $\hat{\boldsymbol{e}}_\xi = \cos(\xi)\hat{\boldsymbol{y}} + \sin(\xi)\hat{\boldsymbol{z}}$, which corresponds to *linear polarization* (LP), where $\boldsymbol{E}$ oscillates along one linear direction (and $\boldsymbol{B}$ oscillates along a line perpendicular to both $\hat{\boldsymbol{e}}$ and $\hat{\boldsymbol{k}}$). There is, however, also the degree of freedom to choose different (complex) phases in the oscillations along $\hat{\boldsymbol{y}}$ and $\hat{\boldsymbol{z}}$. For instance $\hat{\boldsymbol{e}}_\pm = (\hat{\boldsymbol{y}} \pm \mathrm{i}\hat{\boldsymbol{z}})/\sqrt{2}$ corresponds to *circular polarization* (CP), named so because the fields trace out a circle in the plane perpendicular to the direction of propagation. For $\hat{\boldsymbol{e}}_+$, the circle is traced out in a counter-clockwise direction when looking into an oncoming wave, and clockwise for $\hat{\boldsymbol{e}}_-$. Just like $\hat{\boldsymbol{y}}$ and $\hat{\boldsymbol{z}}$ is a basis for the polarization vector, $\hat{\boldsymbol{e}}_+$ and $\hat{\boldsymbol{e}}_-$ also constitute a linearly independent basis which can be used to represent the polarization vector. In general, the polarization is a (complex) linear combination of either the LP or CP basis-vector pair, yielding *elliptical polarization*.

Normalized amplitude and intensity

While the vector-potential formalism is a convenient theoretical tool, in practice $\boldsymbol{A}$ and ϕ are rather impractical for experimental measurements. Even the electric and magnetic fields can be hard to measure directly in a laser pulse, due to their high frequency. Instead, the most common measure of the "strength" of (laser) light is its *intensity*, which measures the radiated power per unit area. The intensity is defined in terms of the fields as

$$I = c\epsilon_0 \left\langle |\mathrm{Re}(\boldsymbol{E})|^2 \right\rangle_\tau, \tag{3.10}$$

where the average $\left\langle |\mathrm{Re}(\boldsymbol{E})|^2 \right\rangle_\tau$ of the squared physical electric field, taken over one laser cycle $\tau = 2\pi/\omega$. Expressed in terms of the amplitudes, the intensity can then be written as

$$I = \begin{cases} \frac{c\epsilon_0\omega^2 A_0^2}{2} = \frac{c\epsilon_0 E_0^2}{2} & \text{for LP,} \\ c\epsilon_0\omega^2 A_0^2 = c\epsilon_0 E_0^2 & \text{for CP,} \end{cases} \tag{3.11}$$

where $E_0 = \omega A_0$ is the amplitude of the electric field. The different expressions for LP and CP are due to the fact that $|\mathrm{Re}(\boldsymbol{E})| = E_0$ stays constant in CP, while it oscillates at twice the wave frequency in LP.

In the context of high-intensity lasers, a *normalized amplitude*

$$a_0 = \left(\frac{2Ie^2}{\epsilon_0\omega m_\mathrm{e}^2 c^3} \right)^{1/2} \approx 0.85 \times \left(\frac{I}{10^{18}\,\mathrm{W\,cm^{-2}}} \right)^{1/2} \left(\frac{\lambda}{1\,\mathrm{\mu m}} \right), \tag{3.12}$$

is used, where $\lambda = 2\pi/\omega$ is the wavelength of the wave. Note that we have here defined a_0 in terms of the intensity, which means that the physical electric and magnetic field amplitudes of the waves differ between linearly and circularly polarized waves with the same a_0. For future reference, we note that, inversely, the intensity can be written as

$$I = \frac{c\epsilon_0}{2} \left(\frac{\omega m_\mathrm{e} c a_0}{e} \right)^2 \approx 1.4 \times 10^{18}\,\mathrm{W\,cm^{-2}} \times a_0^2 \left(\frac{\lambda}{1\,\mathrm{\mu m}} \right)^{-2}. \tag{3.13}$$

3.1.2 Particle motion in an electromagnetic plane wave

The next step in studying the laser–plasma interaction, is to study the particle dynamics inside an electromagnetic plane wave. Instead of the Newtonian formulation with the Lorentz force (2.1), the particle dynamics can also be described using the (relativistic) *Lagrangian* of a particle moving in the vector and scalar potential fields,

$$\mathscr{L} = -mc^2\sqrt{1 - \frac{v^2}{c^2}} + Z^*e(\boldsymbol{v}\cdot\boldsymbol{A} - \phi) = -mc^2\gamma^{-1} + Z^*e(\boldsymbol{v}\cdot\boldsymbol{A} - \phi), \tag{3.14}$$

where m and Z^*e is the rest mass and charge of the particle, respectively, $\boldsymbol{v}$ is its velocity and γ is the Lorentz factor. The motion of the particle is then described via the *Euler–Lagrange equations*

$$\frac{\partial\mathscr{L}}{\partial r_j} - \frac{\mathrm{d}}{\mathrm{d}t}\frac{\partial\mathscr{L}}{\partial v_j} = 0, \tag{3.15}$$

for each coordinate j ($r_j = x$, y and z, and $v_j = v_x$, v_y and v_z).

One advantage of the Lagrangian formalism is that constants of motion arise directly from various symmetries of $\mathscr{L}$. One such constant of motion if the *canonical momentum*,

$$\boldsymbol{P} = \frac{\partial \mathscr{L}}{\partial \boldsymbol{v}} = \boldsymbol{p} + Z^* e \boldsymbol{A} = \gamma m \boldsymbol{v} + Z^* e \boldsymbol{A}, \tag{3.16}$$

where $\boldsymbol{p} = \gamma m \boldsymbol{v}$ is the ordinary (kinetic) momentum. Conservation properties of components of the canonical momentum follow from translational symmetries in the system; for a plane wave, (3.8), $\mathscr{L}$ only depends on the spatial coordinate parallel to $\hat{\boldsymbol{k}}$, $r_\parallel$, hence (3.15) yields that the canonical momentum component perpendicular to $\hat{\boldsymbol{k}}$,

$$\frac{\mathrm{d}\boldsymbol{P}_\perp}{\mathrm{d}t} = \frac{\mathrm{d}}{\mathrm{d}t}\Big[\boldsymbol{p}_\perp + Z^* e \boldsymbol{A}\Big] = 0, \tag{3.17}$$

is conserved. This is true in the case of plane waves, and since modulations in the longitudinal direction do not affect the transverse translational symmetry of the system, $\boldsymbol{P}_\perp$ is also conserved for a longitudinally modulated plane wave. If, however, the wave has additional modulations in the transverse direction, $\boldsymbol{P}_\perp$ is no longer conserved.

Regarding the parallel component of the canonical momentum, its time derivative is also given by (3.15)

$$\frac{\mathrm{d}P_\parallel}{\mathrm{d}t} = \frac{\partial \mathscr{L}}{\partial r_\parallel} = Z^* e \boldsymbol{v} \cdot \frac{\partial \boldsymbol{A}}{\partial r_\parallel}, \tag{3.18}$$

which is generally not zero. However, we may use the *Hamiltonian*,

$$\mathscr{H} = \gamma m c^2 + Z^* e \phi, \tag{3.19}$$

which describes the energy of the system, to derive a conservation relation including $P_\parallel$. Again, in a plane wave with $\phi \equiv 0$, we have

$$\frac{\mathrm{d}\mathscr{H}}{\mathrm{d}t} = \frac{\mathrm{d}}{\mathrm{d}t}\Big[\gamma m c^2\Big]. \tag{3.20}$$

At the same time, the general relation $\mathrm{d}\mathscr{H}/\mathrm{d}t = -\partial \mathscr{L}/\partial t$, with the fact that the plane wave has a time dependence of the form $\boldsymbol{A} = \boldsymbol{A}(kr_\parallel - \omega t)$ and that $\boldsymbol{A}$ is the only time dependence in $\mathscr{L}$, gives

$$\frac{\mathrm{d}\mathscr{H}}{\mathrm{d}t} = -\frac{\partial \mathscr{L}}{\partial t} = +c\frac{\partial \mathscr{L}}{\partial r_\parallel} = c\frac{\mathrm{d}}{\mathrm{d}t}\frac{\partial \mathscr{L}}{\partial v_\parallel} = c\frac{\mathrm{d}P_\parallel}{\mathrm{d}t} = c\frac{\mathrm{d}p_\parallel}{\mathrm{d}t}. \tag{3.21}$$

The last equality stems from the fact that $A_\parallel = 0$, and thus $P_\parallel = p_\parallel + Z^* e A_\parallel = p_\parallel$. Taken together, (3.20) and (3.21), results in the conservation relation

$$\frac{\mathrm{d}}{\mathrm{d}t}\Big[\gamma m c - p_\parallel\Big] = 0, \tag{3.22}$$

which holds for motion in any longitudinally modulated plane wave field ($A_\parallel = 0$), since the longitudinal modulation can be described via an infinite Fourier expansion.

We may now consider a particle initially at rest, $\boldsymbol{p} = 0$, under no influence of any field, $\boldsymbol{A} = 0$, which give the initial values $\boldsymbol{P}_{\perp,0} = 0$ and $p_{\parallel,0} = 0$. If a plane

wave field is slowly (adiabatically) brought up in amplitude, the resulting momenta would be

$$\boldsymbol{p}_\perp = -Z^* e \boldsymbol{A} \tag{3.23a}$$

and

$$p_\parallel = (\gamma - 1)mc, \tag{3.23b}$$

which, through the relativistic energy relation, $(\gamma mc^2)^2 = m^2 c^4 + c^2 (p_\parallel^2 + p_\perp^2)$, gives

$$p_\parallel = \frac{p_\perp^2}{2mc} = \frac{(Z^* e A)^2}{2mc}. \tag{3.23c}$$

Note, however, that these expressions are still highly non-linear, because $\boldsymbol{A}$ depends on the parallel component of the particle trajectory, $r_\parallel$.

As demonstrated, the momentum of a particle moving in a plane wave field is linked to the instantaneous vector potential (in this gauge) felt by the particle. Let us now revisit the normalized amplitude, a_0 defined in (3.12). For an electron, $Z_e^* = -1$ and $m = m_e$, the peak momentum should be $p^{\max} \sim eA_0$, which by combining (3.11) and (3.13) gives

$$p_\perp^{\max} \sim m_e c\, a_0. \tag{3.24}$$

This relation implies that a_0 is a *measure of how important relativistic effects are* for electrons moving under the influence of the wave fields. For $a_0 \ll 1$, relativistic effects can be neglected, while for $a_0 \gtrsim 1$ electrons must be treated relativistically. For a common $800\,\text{nm}$ wavelength, titanium-sapphire laser, $a_0 = 1$ corresponds to an intensity of $2.2 \times 10^{18}\,\text{W\,cm}^{-2}$, which is well within current laser capabilities.

Ponderomotive force

The careful reader may have observed that (3.23b) implies that as soon as the particle is moving, i.e. having any kinetic energy, $U_{\text{kin}} = (\gamma - 1)mc^2 > 0$, it must also have a positive parallel momentum component $p_\parallel > 0$ in the direction of wave propagation. Intuitively, the particle has gained its kinetic energy U_{kin} from the wave and the wave has lost the same amount of energy; then, by the energy–momentum relation for electromagnetic radiation, the wave has also lost the momentum $U_{\text{kin}}/c = (\gamma - 1)mc$, which must have been transferred to the particle – as prescribed in (3.23b).

From this observation, we can conclude that the particle should be drifting along the direction of propagation. The equations of motion in a plane wave, (3.23), may be solved implicitly, which result in that the cycle-averaged longitudinal drift velocity can be computed (Gibbon, 2005; Macchi, 2013)

$$v_\text{d} = \frac{a_0^2}{4 + a_0^2}c, \quad \text{for LP,} \quad \text{and} \quad v_\text{d} = \frac{a_0^2}{8 + a_0^2}c \quad \text{for CP.} \tag{3.25}$$

It follows that there must be a net positive momentum transfer from the wave to the particle, and hence an average force must act in the longitudinal direction, called the *ponderomotive force*. However, since the drift velocity is constant for a constant field amplitude, we must conclude that the ponderomotive force only acts when

the amplitude is changing. In the discussion leading up to (3.23), the plane wave amplitude was said to increase "slowly" from zero to a finite amplitude; it was during this ramp-up in amplitude that the net longitudinal momentum was transferred to the particle.

To find an expression for the ponderomotive force, we study an amplitude modulated plane wave

$$\boldsymbol{A}(\boldsymbol{r}, t) = a(\boldsymbol{r}, t)\boldsymbol{A}_0(\boldsymbol{r}, t) = a(r_\parallel - ct)\, A_0\, \hat{\boldsymbol{e}} \exp[\mathrm{i}(\boldsymbol{k} \cdot \boldsymbol{r} - \omega t)], \qquad (3.26)$$

where a is a slowly varying (compared to the oscillations) *amplitude envelope*, which co-propagates with the wave in the longitudinal direction. Inserting this field into (3.23c) yields

$$\frac{\mathrm{d}p_\parallel}{\mathrm{d}t} = \frac{Z^{*2}e^2}{2mc}\left(A_0^2\frac{\mathrm{d}(a^2)}{\mathrm{d}t} + a^2\frac{\mathrm{d}(A_0^2)}{\mathrm{d}t}\right). \qquad (3.27)$$

Cycle averaging will cancel the $\mathrm{d}A_0^2/\mathrm{d}t$ term, $\langle \mathrm{d}A_0^2/\mathrm{d}t\rangle_\tau = 0$, since that term corresponds to the net force due to a constant amplitude plane wave, which we know must be zero since the drift velocity is constant. As for the $\mathrm{d}a^2/\mathrm{d}t$ term, cycle averaging does not affect it since it changes slowly compared to the oscillation time of the wave. Furthermore, the total derivative may be changed to $\langle \mathrm{d}a^2/\mathrm{d}t\rangle_\tau = \partial a^2/\partial t + v_\mathrm{d}\,\partial a^2/\partial r_\parallel = (1 - v_\mathrm{d}/c)\,\partial a^2/\partial t$. For the purposes of studying the ponderomotive force as the amplitude increases from zero, we may assume that $v_\mathrm{d}/c \ll 1$. The remaining net (ponderomotive) force now becomes

$$F_\mathrm{PM}^\parallel = \left\langle \frac{\mathrm{d}p_\parallel}{\mathrm{d}t}\right\rangle_\tau \simeq \frac{Z^{*2}e^2}{2mc}\left\langle A_0^2\right\rangle_\tau \frac{\partial a^2}{\partial t} = -\frac{Z^{*2}e^2}{2m}\left\langle A_0^2\right\rangle_\tau \frac{\partial(a^2)}{\partial r_\parallel}. \qquad (3.28)$$

For modulations in the transverse direction as well, (3.28) can (with considerable effort[*]) be generalized to

$$\boldsymbol{F}_\mathrm{PM} = -\frac{Z^{*2}e^2}{2m}\left\langle A_0^2\right\rangle_\tau \boldsymbol{\nabla}\!\left(a^2\right) = -\frac{Z^{*2}e^2}{2m\omega^2}\boldsymbol{\nabla}\!\left\langle |\mathrm{Re}(\boldsymbol{E})|^2\right\rangle_\tau = -\frac{Z^{*2}e^2}{2\epsilon_0 cm\omega^2}\boldsymbol{\nabla}I, \quad (3.29)$$

where $I = I(\boldsymbol{r}, t)$ is the modulated intensity, as defined in (3.10). For more details on the derivation of this general expression for the ponderomotive force, the reader is referred to, e.g., the books by Gibbon (2005) or by Macchi (2013); a thorough analytical and numerical treatment of the ponderomotive force in the relativistic regime is also presented by Quesnel & Mora (1998).

From this expression for the ponderomotive force, we can make a few observations. Firstly, the ponderomotive force acts in the same direction regardless of the particle charge, since it only depends on the square of the charge, $(Z^*e)^2$. Secondly, that the ponderomotive force acts to expel particles, away from regions of high intensity, both in the transverse direction, and longitudinally when the intensity is increasing. Thirdly, while the ponderomotive force acts independently of the sign of the charge, it will still affect electrons more than ions, since F_PM is inversely proportional to the particle mass. In summary, the ponderomotive force will mainly affect the electrons in a plasma, by pushing them away from regions of high intensity.

---

[*]One of the more major challenges in this generalization is that (3.23c) no longer holds, since $A_\parallel \neq 0$ for transversely modulated waves.

3.1.3   Laser interaction with a plasma

The above single-particle dynamics can be translated to, and guides the understanding of, laser–plasma interactions. However, since the particles in the plasma collectively affect the macroscopic fields, the interaction is manifestly non-linear in both the plasma and field dynamics. One of the major changes here is in the equations for the field, (3.6), which are no longer homogeneous – i.e. ρ and $\boldsymbol{j}$ are no longer zero. We may still, however, search for a plane wave solution, albeit with a different dispersion relation between k and ω. We take our starting point by introducing the complex exponential form of the vector potential, (3.8), and inserting it into (3.6b), which gives

$$k^2 \boldsymbol{A} - \frac{\omega^2}{c^2} \boldsymbol{A} = \mu_0 \boldsymbol{j}. \tag{3.30}$$

The presence of the term on the right hand side is what changes the dispersion relation. We must now calculate the current density, $\boldsymbol{j}$, in terms of $\boldsymbol{A}$.

While $\boldsymbol{j}$ can certainly be calculated using the distribution function, as in (2.16b), for the purposes of this discussion, we may make some simplifying assumptions: (i) we assume that the field strength is sufficiently weak, so that the dynamics can be described non-relativistically; (ii) since the ions are much heavier than the electrons, we assume that $\boldsymbol{j} = \boldsymbol{j}_\mathrm{e} = -en_\mathrm{e}\boldsymbol{v}_\mathrm{e}$, i.e. that all the current stems from the electrons; (iii) since the intensity is low, we can neglect the ponderomotive force and the induced longitudinal drift, i.e. $\boldsymbol{v}_\mathrm{e}$ is purely in the transverse plane. With the first and third assumption, we can write the electron (transverse) flow velocity as

$$\boldsymbol{v}_\mathrm{e} = \frac{\boldsymbol{p}_{\mathrm{e},\perp}}{m_\mathrm{e}} = +\frac{e\boldsymbol{A}}{m_\mathrm{e}}. \tag{3.31}$$

Taken together with the second assumption, we can now write (3.30) as

$$k^2 \boldsymbol{A} - \frac{\omega^2}{c^2} \boldsymbol{A} = -\mu_0 \frac{e^2 n_\mathrm{e} \boldsymbol{A}}{m_\mathrm{e}} = -\frac{e^2 n_\mathrm{e} \boldsymbol{A}}{c^2 \epsilon_0 m_\mathrm{e}}, \tag{3.32}$$

which gives the dispersion relation

$$c^2 k^2 = \omega^2 - \frac{e^2 n_\mathrm{e}}{\epsilon_0 m_\mathrm{e}} = \omega^2 - \omega_\mathrm{p}^2, \tag{3.33}$$

where

$$\omega_\mathrm{p} \equiv \sqrt{\frac{e^2 n_\mathrm{e}}{\epsilon_0 m_\mathrm{e}}} \tag{3.34}$$

is called the *plasma frequency.*

The plasma frequency measures how fast the plasma can respond to electromagnetic perturbations. A major consequence of the dispersion relation, (3.33), is the fact that for $|\omega| < \omega_\mathrm{p}$, k becomes imaginary, and there can be no propagating waves. This means that a laser pulse impinging on a plasma will be reflected if the laser frequency, ω, is lower than the plasma frequency. In practice, the laser frequency is fixed, while the target plasma changes, so instead of comparing the laser and plasma frequency, the plasma density is compared to the critical density

$$n_\mathrm{c} \equiv \frac{\epsilon_0 \omega^2 m_\mathrm{e}}{e^2}, \tag{3.35}$$

where ω is the laser/reference (angular) frequency. A plasma is thus said to be *underdense* when $n_e < n_c$ or *overdense* when $n_e > n_c$, meaning that the plasma (partially) transmits or reflects the incoming wave, respectively. This is a basic classification of laser-plasmas.

Laser interaction with an overdense plasma

The work in this thesis has been centered around various effects of collisions in laser-plasma scenarios, and since collisions are more prominent in higher-density plasmas, the work here is focused on overdense plasmas. We will therefore take a few moments to look into some of the specifics of the interaction between the laser light and an overdense plasma.

As noted, laser light (in general) cannot propagate through an overdense plasma, as demonstrated by the dispersion relation (3.33). However, the fact that k becomes imaginary for $\omega < \omega_p$ does not mean that the field does not penetrate the overdense region at all. There will be an evanescent field with an exponentially decaying amplitude profile. For a normally incident laser on a semi-infinite plasma occupying the space $x \geq 0$, we have an amplitude profile inside the plasma that is proportional to

$$A_{\mathrm{plasma}}(x) = A_1 \exp(-x/l_s), \tag{3.36}$$

where l_s is called the *skin-depth* and is given by

$$l_s = \frac{c}{\omega_p}\left(1 - \frac{\omega^2}{\omega_p^2}\right)^{-1/2} = \sqrt{\frac{\epsilon_0 m_e c^2}{e^2 n_e}}\left(1 - \frac{\omega^2}{\omega_p^2}\right)^{-1/2} = \frac{\lambda}{2\pi}\sqrt{\frac{n_c}{n_e}}\left(1 - \frac{n_c}{n_e}\right)^{-1/2}, \tag{3.37}$$

where λ is the laser wavelength (in vacuum). For highly overdense plasmas, $n_e \gg n_c$, the parenthetical factor may be neglected and the skin-depth can be approximated as $l_s \simeq c/\omega_p$.

Next, we still consider a normally incident laser on a sharp vacuum–plasma boundary at $x = 0$, and since the light is reflected from the plasma, a standing wave is generated which will have an amplitude profile of

$$A_{\mathrm{vacuum}}(x) = 2A_0 \sin(-kx + \varphi), \tag{3.38}$$

where A_0 is the amplitude of the incoming wave, $k = 2\pi/\lambda$ is the vacuum wavenumber and φ is a constant phase. By matching the values and slopes of (3.36) and (3.38) at $x = 0$, we get (after some algebraic and trigonometric manipulations) the amplitude relation and phase as

$$\begin{cases} A_1 = 2A_0(n_c/n_e)^{1/2}, \\ \tan\varphi = kl_s = (n_c/n_e)^{1/2}(1 - n_c/n_e)^{-1/2}. \end{cases} \tag{3.39}$$

The full vector potential is thus

$$\boldsymbol{A} = -\mathrm{i}A(x)\hat{\boldsymbol{e}}\exp(-\mathrm{i}\omega t) = -2\mathrm{i}A_0\hat{\boldsymbol{e}}\exp(-\mathrm{i}\omega t) \times \begin{cases} \sin(-kx + \varphi), & x < 0, \\ \left(\frac{n_c}{n_e}\right)^{1/2}\mathrm{e}^{-x/l_s}, & x \geq 0, \end{cases} \tag{3.40}$$
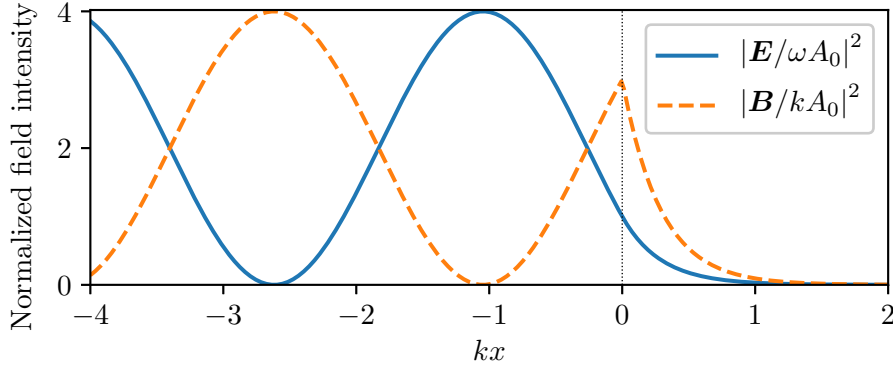
Figure 3.1: Illustration of the standing wave field intensity for a plane wave field normally incident on a plasma occupying the space $x \geq 0$ with density $n_\mathrm{e} = 4n_\mathrm{c}$, giving a skin-depth of $kl_\mathrm{s} \approx 0.6$. Note the discontinuity in the gradient of the amplitude of the B field.

which gives the fields as

$$\boldsymbol{E} = -\frac{\mathrm{d}\boldsymbol{A}}{\mathrm{d}t} = \omega A(x)\hat{\boldsymbol{e}}\exp(-\mathrm{i}\omega t), \tag{3.41}$$

and

$$\boldsymbol{B} = \boldsymbol{\nabla} \times \boldsymbol{A} = -\mathrm{i}\frac{\partial A}{\partial x}\hat{\mathbf{x}} \times \hat{\boldsymbol{e}}\exp(-\mathrm{i}\omega t). \tag{3.42}$$

An example of such standing wave fields is shown in Fig. 3.1, where the normalized field intensity of E and B are plotted. Note the discontinuity in the gradient of the B field amplitude at $x = 0$, which is due to the discontinuity in $\boldsymbol{j}$ at the surface of the plasma.

The standing wave discussed here gives some important insights: (i) the laser field penetrates the overdense plasma over a few skin-depths, l_s; (ii) the on-target intensity, at the plasma surface, is a factor $(A_1/A_0)^2 = 4n_\mathrm{c}/n_\mathrm{e}$ lower than the free-propagating laser intensity. However, this description only takes into account the effect of a cold-fluid (zero thermal spread) plasma on the electromagnetic wave. Whereas, in reality, the laser radiation to a high degree affects the plasma as well. Most notably, the ponderomotive force, (3.29), will push mainly the electrons deeper into the plasma, which sets up a *charge-separation layer* and a static electric field which accelerates the ions remaining in the layer into the target.

Another effect not captured by the description above, is the fact that the plasma has an internal pressure. So just like a regular gas, the plasma will try to *hydrodynamically* expand into the vacuum region, thus creating a *preplasma*, which more slowly ramps up in density – from under- to overdense – thus the laser–plasma interaction is not necessarily that of a sharp vacuum–plasma boundary. The creation of a preplasma is linked to the fact that the (main) laser pulse is usually preceded by a *pre-pulse* due to an amplification of parasitic spontaneous emission in the laser system. While the main pulse can be as short as a few tens of femtoseconds, the pre-pulse may last for as long as nanoseconds, thus pre-heating the plasma on a hydrodynamical time scale, during which the plasma would significantly expand and change its shape and density profile.

There are, of course, additional processes at play, some of which will be discussed later on, such as particle acceleration and plasma heating, while others will be left for other works in the field, e.g. the book by Gibbon (2005). We will, however, conclude this section by mentioning one last laser-plasma effect which can occur in overdense plasmas: *relativistic transparency* – described clearly in the paper by Siminos *et al.* (2012) – where due to the "relativistic mass effect", $m_e \to \gamma m_e$, the effective critical density is increased, which may then permit transmission of the laser pulse at higher intensities.

3.2 Laser-based heating of overdense plasmas

Perhaps the most basic outcome of irradiating a target with a high-intensity laser wave is that the target gets hot. However, an interesting consequence of the momentum relations in (3.23) is that once the laser pulse has passed, and $\boldsymbol{A}$ has returned to zero[†], the energy of the free particle also returns to zero, i.e. no net energy was transferred from the field to the particle. This result, however, only holds in a single propagating plane wave, and not in the standing wave established outside of the reflective plasma, or in the evanescent wave inside of it.

On an abstract level, there are three paths that a laser pulse will take in the interaction with a plasma: *reflection*, *transmission* or *absorption*. Assuming that the plasma is sufficiently thick and overdense, we can neglect any transmission. It would therefore be useful to briefly overview the reason why an overdense plasma reflects radiation. From the previous discussion in §3.1.3, we learned that if $\omega_p > \omega$, the electrons can react fast enough to collectively prevent the laser light from shining through the plasma. When the electrons are reacting to the laser field, they are oscillating with it. By doing so, the electrons also radiate a "response field" themselves, as they are now accelerating charges. The response field is emitted both forward and backward (with respect to the propagation direction of the laser radiation); the forward-propagating response field is phase-shifted from the laser field and acts to cancel it, while the backward-propagating response field *is* the reflected laser field. Mechanisms which alter or impede the co-oscillation of the electrons with the laser field, will therefore affect their ability to reflect the field and thus allow for absorption of the laser energy.

3.2.1 Skin heating mechanisms – inverse bremsstrahlung, sheath inverse bremsstrahlung, normal and anomalous skin effects

The first mechanism that comes to mind that makes the electron oscillation less coherent might be that of collisions. Typically, the much heavier ions will act as a stationary background with which the oscillating electrons collide. In the collisions

---

[†]The observant reader will have noted that just because the laser pulse has a finite duration, i.e. $\boldsymbol{E}(t\to\infty) = 0$, that does not necessarily imply that $\boldsymbol{A}(t\to\infty) = 0$ since $\boldsymbol{A}(t) = -\int_{-\infty}^{t} \boldsymbol{E}(t')\,\mathrm{d}t$. If $\boldsymbol{A}(t\to\infty) \neq 0$, that would mean that $\boldsymbol{E}$ has a zero-frequency component, which would violate Gauss's law (2.15a) in vacuum.

with the ions, pitch-angle scattering dominates, which diffuses the oscillatory response of the electrons to the laser field, thus causing absorption. Such collisionally induced radiation absorption has been given the somewhat misleading name of *inverse bremsstrahlung*, after the "regular bremsstrahlung" effect which occurs when an electron emits a photon due to a change in trajectory caused by a collision with an ion.

In the case of a steep vacuum–plasma interface, the field inside the plasma is evanescent, with an exponentially decaying amplitude inside the *skin layer* of thickness $\sim l_\mathrm{s}$. Under these circumstances the heating is concentrated to the skin layer, and heat is then transferred deeper into the plasma by the heated electrons. The prototypical collisional skin heating mechanism is the *normal skin effect*, where the electron–ion collisional mean free path is shorter than the skin-depth, $\lambda_\mathrm{ei} \lesssim l_\mathrm{s}$, and the corresponding collision frequency is greater than the laser frequency, $\nu_\mathrm{ei} \gtrsim \omega$. Normal skin effect heating occurs due to collisions that strongly affect the trajectories of the electrons when they are moving under the influence of the laser field in the skin region. However, due to the collisionality decreasing with particle energy, the conditions for normal skin effect are seldom met in a high-intensity ($a_0 \gtrsim 1$) experiment. An extensive analytical study of the normal and anomalous (to be discussed) skin effects can be found in the paper by Rozmus & Tikhonchuk (1990).

Collisionless skin-layer heating

It is important to note that the individual electrons in the plasma also travel longitudinally. In the skin layer, the $\boldsymbol{v} \times \boldsymbol{B}$ term of the Lorentz force will accelerate the electrons in the longitudinal direction further into the plasma (ponderomotive force[‡]). Likewise, thermal motion of the electrons deeper in the plasma means that there are always new electron replenishing the skin layer, coming in with a velocity close to the thermal speed, $v_\mathrm{te} = (T_\mathrm{e}/2m_\mathrm{e})^{1/2}$. In the case of the normal skin effect, collisions are strong enough ($\lambda_\mathrm{ei} \lesssim l_\mathrm{s}$) to significantly affect this longitudinal electron exchange and cause heating. However, even without strong collisionality, there are mechanisms that allow for laser-energy absorption.

One such case is when the transit time for an electron coming from inside the plasma and being reflected back from the skin region, $\sim l_\mathrm{s}/v_\mathrm{te}$, is shorter than a laser cycle, i.e. $\omega l_\mathrm{s}/v_\mathrm{te} \lesssim 1$. The electron may then be energized in the transverse plane by the laser field near the front, and due to the reflection at the charge-separation potential, it can bring some of that transverse momentum with it deeper into a weak-field region inside the plasma. By bringing the transverse momentum deeper into the plasma and shifting the position where they radiate the response field deeper into the plasma, the electrons effectively increase the penetration depth of the laser, thus increasing the absorption. This effect is called the *anomalous skin effect*, and is described in detail by (Rozmus & Tikhonchuk, 1990), together with the normal skin effect.

[‡]While the ponderomotive force as described in (3.29) is formally a cycle-averaged force from the radiation, the periodically oscillating longitudinal force from the laser pulse is often also simply referred to as the ponderomotive force. In this case, the cycle averaging is ignored and the ponderomotive force is simply taken as $F_\mathrm{PM}(\boldsymbol{r}, t) \propto \boldsymbol{\nabla}(|\mathrm{Re}[E(\boldsymbol{r}, t)]|^2)$.

Another, rather similar, mechanism is the *sheath inverse bremsstrahlung*, first introduced by Catto & More (1977). Like the anomalous skin effect, sheath inverse bremsstrahlung also operates on the principle that the electrons coming from inside the plasma are reflected at the front. However, here the skin layer transit time is longer than the laser cycle, $\omega l_\mathrm{s}/v_\mathrm{te} \gtrsim 1$, yet the reflection time in the front is still short compared to the laser cycle. The long transit time means that the energy of the reflected electron is adiabatically increased, on average, by the oscillating laser field, such that the electron brings with it more energy into the plasma than it had leaving it.

3.2.2 Resonant and not-so-resonant heating

So far, we have only discussed laser-based heating in targets with a sharp plasma–vacuum interface. While, in practice, pre-pulse heating may cause hydrodynamical plasma expansion, leading to a smooth density transition from under- to overdense. In that case the laser most strongly interacts with the plasma at the *critical surface*, i.e. at the depth where $n_\mathrm{e} = n_\mathrm{c}$. For normal incidence, the interaction is similar to what is described above in § 3.2.1, however, the picture changes for oblique incidence[§].

Consider a semi-infinite plasma which has a density ramp around $x = 0$ with a gradient along the x-direction. The laser impinges on the plasma obliquely, at an angle θ from the normal in the xy-plane, i.e. the wave vector is $\boldsymbol{k} = k(\cos\theta\hat{\mathbf{x}}+\sin\theta\hat{\mathbf{y}})$. The (linear) polarization, $\hat{\boldsymbol{e}}$, can be chosen from two LP basis vectors, $\hat{\boldsymbol{e}}_s = \hat{\mathbf{z}}$ and $\hat{\boldsymbol{e}}_p = \sin\theta\hat{\mathbf{x}} - \cos\theta\hat{\mathbf{y}}$, corresponding to the so called *s-* and *p-polarizations*, respectively.

In the case of a *p*-polarized laser wave, the electric field has a component in the x-direction which will drive the plasma to oscillate along the density gradient, giving rise to density waves. The laser wave is reflected at a depth where $n_\mathrm{e} = n_\mathrm{c}\cos^2\theta$, but given the right circumstances (not too flat nor to steep density profile), the component of the laser electric field normal to the plasma surface will reach into the depth where $\omega_\mathrm{p} = \omega$, where it is resonant with, and will excite, the *Langmuir* plasma-wave mode. The excited Langmuir wave can penetrate deep into the plasma where it dissipates its energy, e.g. via collisional damping. This energy-transfer mechanism is simply called *resonant absorption*, due to the resonant excitation of the Langmuir wave.

Resonant absorption relies on a long scale length for the density variation in order to drive the Langmuir wave deeper into the plasma than the laser penetrates. For shorter density scale lengths, comparable to the oscillation amplitude of the electrons driven by the x-component of the laser electric field, the excitation of the Langmuir wave mode is no longer as efficient. However, another phenomenon occurs in this scenario: the electrons oscillating near the critical surface will move towards lower-density regions, where they will experience stronger fields and can be accelerated to high energies before they are pushed back into the plasma, where they

---

[§]Note that the effects discussed in § 3.2.1 also work for oblique incidence. Indeed, the skin heating mechanisms often have better absorption efficiently for oblique incidence than for normal incidence.

can dissipate the energy gained in the vacuum/low-density region. This mechanism was named *not-so-resonant, resonant heating* by Brunel (1987) who discussed it as a problem for an electron acceleration scheme; others have since taken to calling this mechanism either "vacuum heating" (which we will use for a similar mechanism discussed below) or simply the "Brunel mechanism".

3.2.3 "$j{\times}B$" and vacuum heating

Due to the velocity dependence of the magnetic force term in the Lorentz force, the effects of the magnetic field can usually be neglected as long as the electrons are non-relativistic, $v \ll c$. In relativistic laser pulses, $a_0 \gtrsim 1$, the electrons are relativistic, and the magnetic field effects may become important. One absorption mechanism based on such effects is the so called "$j{\times}B$ *heating*", first described by Kruer & Estabrook (1985). This mechanism is similar to the resonant and not-so-resonant heating in that electrons are oscillating back and forth, but instead of relying on the E_x component of an obliquely incident p-polarized wave, the $j{\times}B$ mechanism works for both p- and s-polarized laser pulses, and even at normal incidence. The longitudinal oscillation is instead driven by the $\boldsymbol{v} \times \boldsymbol{B}$ term of the Lorentz force. Note that since both $\boldsymbol{v}$ and $\boldsymbol{B}$ oscillates with a frequency ω, the product will oscillate at twice the laser frequency, 2ω. Traditionally the $j{\times}B$ heating refers to the heating from oscillations within the skin depth of the plasma.

There is, however, an effect similar to the not-so-resonant heating mechanism for sharp plasma boundaries, where electrons that exit the plasma can be accelerated transversely by the laser electric field before being pushed back in by the $\boldsymbol{v} \times \boldsymbol{B}$ force. We refer to this mechanism as *vacuum heating*, as described by Bauer & Mulser (2007) and May *et al.* (2011). Vacuum heating relies on the temporal modulation of the ponderomotive force, which periodically pushes the electrons into the plasma, at twice the laser frequency; the electrostatic field from the bare ions left behind then pulls the electrons back. In this oscillation, electrons with the right trajectories will continue out as far as $\lambda/4$ into the vacuum region where the electric field of the standing wave peaks, and hence where they will be most efficiently accelerated. These electrons can be observed as *bunches of high-energy electrons* produced at twice the laser frequency.

One important note for both these mechanisms is that *neither $j{\times}B$ nor vacuum heating work with circular polarization*, since they rely on the oscillating ponderomotive force, $F_{\mathrm{PM}}(\boldsymbol{r}, t) \propto \boldsymbol{\nabla}(|\mathrm{Re}[E(\boldsymbol{r}, t)]|^2)$. With CP, the strength of the fields are constant (up to their slow amplitude modulation), the ponderomotive force thus only produces a steady push inward. Since the B field strength is also constant, the electrons cannot reach further than approximately one Larmor radius $\sim m_{\mathrm{e}} v_{\mathrm{te}}/(e B_1) \simeq \lambda v_{\mathrm{te}}/(4\pi c a_0) \ll \lambda/4$, where B_1 is the magnetic field strength at the plasma surface.

3.3 Laser-induced plasma heating

One of the direct applications of laser-based plasma heating is the creation of warm/hot dense matter (W/HDM). Here, the sudden and short-duration energy

transfer from a high-intensity laser pulse is employed to quickly heat up the target *isochorically*, i.e. "at constant volume", before the plasma has time to hydrodynamically expand. As discussed in the introduction to this thesis (§ 1.2), isochoric heating is used to create W/HDM which has many further applications.

Looking back at what has been conducted so far, most laser-based isochoric heating experiments have exploited high-energy electrons generated by the laser (Martinolli *et al.*, 2006; Chen *et al.*, 2007; Nilson *et al.*, 2010; Pérez *et al.*, 2010; Santos *et al.*, 2017; Sawada *et al.*, 2019). The fast electrons are generated by mechanisms similar to $j{\times}B$ and vacuum heating, and are driven by a linearly polarized laser. These electrons then heat the plasma bulk to high temperatures ($0.1-1\,\mathrm{keV}$), while the plasma remains at solid-range densities. The heating of the plasma is caused by the interaction of the fast electrons with the bulk plasma via various mechanisms. The most direct mechanism is heating via collisions between the fast electrons and the background plasma (Robinson *et al.*, 2014); although, due to the decreasing collisionality with temperature and particle energy, this mechanism gets increasingly weaker for higher electron energies and as the plasma is heated. When the fast electrons rush into the plasma, there is also a return current of slower electrons to ensure quasi-neutrality; ohmic (collisional) dissipation of this return current will also contribute to heat the bulk plasma (Lovelace & Sudan, 1971; Guillory & Benford, 1972; Bell & Kingham, 2003; Robinson *et al.*, 2014). Lastly, since the fast electrons come in bunches at a fixed frequency double that of the laser, the fast-electron bunches can drive plasma waves which are collisionally damped and dissipated as heat (Sherlock *et al.*, 2014).

Usually, however, the heating from fast electrons results in poor spatial uniformity (Dervieux *et al.*, 2015) and relatively slow thermalization ($\sim$ps). The slow thermalization of the fast electrons is simply a consequence of the decreased effects of collisions at higher energies. However, because some applications – such as verification of high-energy-density (HED) atomic physics models (Hoarty *et al.*, 2013*a*; Faussurier & Blancard, 2019) or HED states of matter models (Renaudin *et al.*, 2003; Nettelmann *et al.*, 2008) – may require a well-thermalized, Maxwellian plasma, the fast-electron methods may not be ideal since the timescale for thermalization can be comparable to that of hydrodynamic expansion. One of the motivations behind the work in paper B was to examine a way of generating well-thermalized, solid-density plasmas.

3.3.1 Revisiting inverse bremsstrahlung

As previously notes, efficient creation of fast-electron bunches requires a linearly polarized laser pulse (at least for normal laser incidence). So by using CP instead, one can suppress the creation of the fast electrons and thus the problem of slow thermalization. However, that also removes one of most effective channels of energy transfer from the laser to the plasma. In paper B, we study the heating and thermalization of the plasma using 1D PIC simulations. By staying in one dimension, the laser is necessarily normally incident, so there is also no possibility of resonant or not-so-resonant absorption. We are therefore left with inverse bremsstrahlung as the main heating mechanism. Since inverse bremsstrahlung is a purely collisional
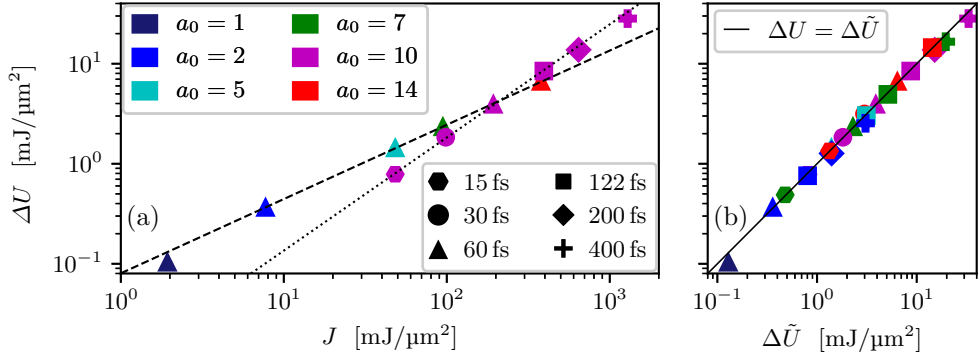
Reproduced from Sundström *et al.* (2020*a*) (cc)(i) 4.0

Figure 3.2: Total simulated kinetic energy gain ΔU against (a) the laser energy J for different combinations of laser parameter a_0 and full-width at half-maximum pulse duration t_{FWHM}, and (b) the inferred power-law scaling $\Delta \tilde{U} \propto a_0^{1.48} t_{\text{FWHM}}^{1.13}$.

mechanism, thermalization happens on a comparable timescale.

While inverse bremsstrahlung is usually dismissed at high laser intensities, due to the decreasing collisionality at higher particle energies, it can be increased by using high-Z ions. Since the electron–ion collision frequency scales as the square of the ion charge, $(Z^*)^2$, the plasma can be made sufficiently collisional for inverse bremsstrahlung to play a significant role in the laser-energy absorption. Furthermore, the collision frequency is also proportional to the plasma density, thus collisions may not immediately be neglected in solid laser targets. Indeed, for solid-density copper targets ($Z^* = 27$), studied in paper **B**, the bulk electron temperatures were found to be essentially equal between CP and LP, which indicates that a majority of the laser energy was absorbed via inverse bremsstrahlung – even with LP. The main difference between LP and CP was however in the high-energy end of the electron energy spectra, where the fast electrons generated by LP created a high-energy tail that was slow to thermalize.

As a part of the study of the inverse bremsstrahlung heating, we performed scans in laser intensity (a_0) and pulse full-width at half-maximum duration t_{FWHM} (Gaussian temporal intensity profile). Figure 3.2 is reproduced from paper **B** and it shows in panel (a) the scaling of the gained kinetic energy of the particles in the plasma, ΔU, plotted against the laser pulse energy, J. From the power laws in a_0 and t_{FWHM}, a combined empirical power-law relation was inferred:

$$\Delta \tilde{U} \propto a_0^{1.48} \left(\frac{t_{\text{FWHM}}}{100 \, \text{fs}} \right)^{1.13}. \tag{3.43}$$

This scaling law was then confirmed against a wider range of combinations of various a_0 and t_{FWHM} in Fig. 3.2b. An observation regarding this power-law scaling, is that the absorption *efficiency*, $\Delta \tilde{U}/J \propto \Delta \tilde{U}/(a_0^2 t_{\text{FWHM}})$, scales as $a_0^{-0.52} \times t_{\text{FWHM}}^{0.13}$, which means that longer-duration and lower-intensity pulses are favored for the same pulse energy, J.

Effects of ionization

Since the ionization level, Z^*, plays a crucial role in the collisionality of the plasma, and thus also the heating, it is necessary to have a good understanding of it to correctly model and simulate the collisional plasma heating. We study this through a simulation with self-consistent ionization, via collisional impact ionization and field ionization (Pérez *et al.*, 2012). The laser field is found to quickly ionize the ions at the irradiated surface of the target to $Z^* \gtrsim 20$. Later, collisional impact ionization gradually brings up the ionization level to $Z^* \simeq 27$ in the bulk of the plasma. Importantly, since the ionization quickly reaches relatively high levels in the skin region, where the absorption happens, the assumption of $Z^* = 27$ in the other simulations is justified for studying the absorption efficiency.

However, a side-effect of the field ionization is that a population of high-energy electrons is created. Indeed, electrons originating from ions in the charge-separation layer, are "injected" into a region of strong laser field, and are energized in a manner similar to the vacuum heating mechanism with LP. Subsequently, the self-consistent ionization simulation produced a less thermalized plasma than its fixed-ionization counterpart.

3.4 Collisional effects on electrostatic shocks

As discussed in the introduction (§ 1.1), laser-based ion acceleration has promising potential to supplement or replace conventional acceleration methods. In particular, collisionless shock acceleration (CSA) has potential to produce a ion beam with a narrow energy spread, which could potentially be used in medical applications. Electrostatic shocks are, however, challenging to create in a reproducible fashion. One of the main problems to overcome towards this goal is to understand the shock formation process.

A shock wave is characterized by a disturbance propagating faster than the speed of sound, so that the *upstream* plasma does not have time to react to the shock before it arrives. The shock therefore results in rapid compression along with fast acceleration of the plasma to the speed of the shock in the *downstream* plasma. In this process, the directional kinetic energy of the shock is also dissipated into thermal energy as the plasma passes the shock front. The dissipation can take place either through collisional processes – as in hydrodynamic shocks – or via collisionless mechanisms, involving longitudinal electrostatic fields generated by space charge effects from shock compression. In the case of collisionless electrostatic shocks, some of the ions hitting the shock front are reflected and accelerated to twice the shock velocity in the lab frame, and thus provide a dissipation path for the formation and continued propagation of the shock.

While "collisionless shocks", as the name suggests, are sustained by collisionless, collective plasma processes, inter-particle collisions are never truly zero, in a real plasma. Indeed, collisions may even affect the dynamics of the shocks in various ways depending on the strength of the collisionality. In this section we will take a look at some such effects, studied in paper **A** and **C**. In the former, we study a semi-analytical model of electrostatic shocks and investigate the effects of perturbatively
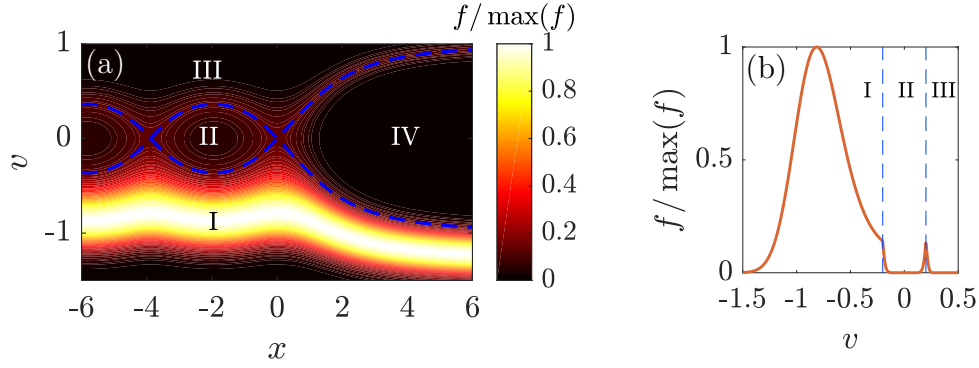
Figure 3.3: Phase-space density plot of the ion distribution function (a) and a slice of the ion distribution in the velocity plane at $x = -0.62$. The spatial coordinate, x, is normalized to the Debye length, $\lambda_\mathrm{D} = [\epsilon_0 T_\mathrm{e}/(e^2 n_{\mathrm{e},0})]^{1/2}$, where $n_{\mathrm{e},0}$ is the far-upstream electron density, and the velocity coordinate, v, is measured in the co-moving frame of the shock wave and normalized to the ion-acoustic speed, $c_\mathrm{s} = (Z_\mathrm{i} T_\mathrm{e}/m_\mathrm{i})^{1/2}$. The dashed curves represent phase-space separatrices, separating the four distinct regions of phase space: passing (I), trapped (II), co-passing (III) and reflected (IV).

introducing a weak collisionality to that model. In the latter, electrostatic shocks and shock formation is studied in solid-density high-Z^* materials via PIC simulations; these materials are, as discussed in § 3.3.1, among the most collisional types of laser-plasmas, and should therefore be strongly affected by collisions.

3.4.1 Weakly collisional electrostatic shock model

The weakly collisional shock model studied in paper **A** is a kinetic, quasi-steady-state model of an electrostatic shock, built upon the model by Cairns *et al.* (2014, 2015) and Pusztai *et al.* (2018). The model is kinetic, one-dimensional (1D) and non-relativistic; it self-consistently calculates the electrostatic potential, $\phi(x)$, and the ion distribution function, f, given the input parameters: shock Mach number, $\mathcal{M}$, the electron-to-ion temperature ratio, $T_\mathrm{e}/T_\mathrm{i}$, and the ion charge number Z^*. The core of the (collisionless) model is based upon the circumstance that ions, which follow constant-energy trajectories in the frame co-moving with the shock, either pass the potential barrier of the shock or are reflected, depending on which region of phase space they belong to. These regions are: (I) the *passing region*, in which the ions have sufficient kinetic energy in the shock frame to pass the shock front into the downstream; (II) the *trapped region*, comprised of the islands in phase space where ions would be trapped due to electrostatic potential oscillations downstream of the shock; (III) *co-passing region*, the region from which ions can overtake the shock and pass into the upstream; and last (IV) the *reflected region*, in which the ions are reflected at the shock front. These regions are separated by a *separatrix* marked out in Fig. 3.3a.

In the original collisionless model, phase-space regions II and III would be completely devoid of ions. All ions coming in from the far upstream are in either region I or IV. Since the ions cannot cross the separatrix without collisions, there will be a

discontinuity in the distribution function between region I and II as well as between IV and III. This discontinuity will be highly susceptible to diffusion. Collisional effects, in paper **A**, were therefore added by including a velocity-diffusion collision operator near the line of discontinuity, which permitted a steady diffusion of ions into regions II and III. Ions entering the trapped region (II) would then occupy a growing boundary layer of region II near the separatrix to region I, and circulate to fill a symmetric boundary layer near the separatrix to region III, which they would also be able to cross. All in all, the distribution would look similar to that in Fig. 3.3, where panel (a) displays the distribution in phase space, and panel (b) shows a slice of the distribution in the downstream. Note the symmetry of the distribution in region II in Fig. 3.3b.

The practical results of this diffusion of ions into the trapped and co-passing regions of phase space is that the downstream potential oscillations grow deeper at a rate roughly proportional to $\sqrt{\nu t}$, where νt is dubbed the *collisional age* of the shock. The importance of this observation is that, since shocks can be long-lived, even though the collisional time scale, $\simeq 1/\nu$, is much slower than the ion time scale of the shock, λ_D/c_s, collisions may affect the shock if the collisional age becomes order unity or larger, $\nu t \gtrsim 1$.

Note that, the analysis in paper **A** starts with the assumption that the collisionality is indeed perturbatively small, $\nu \ll c_s/\lambda_D$, and as such, the model is limited to these – close to collisionless – cases. The opposite limit is to study hydrodynamic shocks, which are completely dominated by the effects of collisions. The intermediary parameter region, where the physics require kinetic modeling and collisions are still important, is far less explored than either of these extremes. While the work in paper **A** has approached this gap in the intermediary region from the collisionless side, there has also been efforts at approaching from the strong-collisionality side of the gap (Thomas *et al.*, 2012; Keenan *et al.*, 2018). The following sub-section in this thesis will discuss another study of stronger collisional effects on shocks.

3.4.2 Laser-generated electrostatic shocks in more strongly collisional laser-plasmas

The collisional model in paper **A** only considers single-ion-species ion–ion collisions. The work in paper **C** was therefore originally motivated by the work by Turrell, Sherlock & Rose (2015), where the effects of collisions were studied in a plasma with multiple ion species (caesium hydride, or CsH) target. Since the shock is electrostatic, when there are multiple ion species present, the *charge-to-mass ratios*, Z^*/A where A is the (dimensionless) atomic mass number, of the ion species play a crucial role in their interaction with the shock. Notably, hydrogen ions (protons) have a charge-to-mass ratio of 1, while almost every other ion species have $Z^*/A \lesssim 0.5$, which means that hydrogen, when present, will be preferentially reflected by the shock at a significantly larger fraction of the proton population (Pusztai *et al.*, 2018). In the case of CsH, one would therefore expect the hydrogen ions to be reflected to a much higher degree than the Cs^{27+} ions, with $Z^*/A \approx 0.2$, if collisions were to be neglected.

Another result from the semi-analytical model, first noted by Cairns *et al.* (2015),
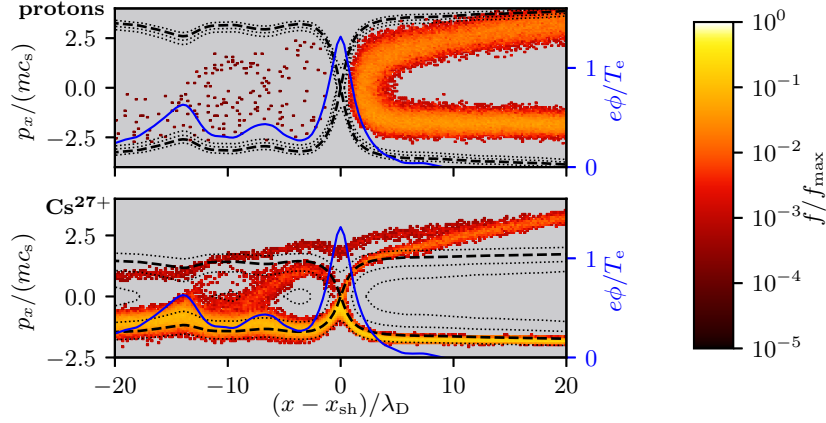
Figure 3.4: Proton (top panel) and Cs ion (bottom panel) distributions in the shock frame of reference, $\simeq 25\,\mathrm{fs}$ after the laser pulse has ended, together with the shock electrostatic potential, $e\phi/T_\mathrm{e}$ (blue solid line, right axes), with $T_\mathrm{e} = 10\,\mathrm{keV}$. Also shown are contours of constant energy, $\mathcal{E} = mv^2/2 + eZ(\phi - \phi_\mathrm{max})$ (black, dashed or dotted lines). The black dashed line is related to the separatrix in the model discussed in §3.4.1.

is that $T_\mathrm{e} \gg T_\mathrm{i}$ in order for the shock to exist. This requirement is linked to the fact that the sound speed, $c_\mathrm{s} = (Z^* T_\mathrm{e}/m_\mathrm{i})^{1/2}$, must be significantly larger than the ion thermal speed, $v_\mathrm{ti} = (T_\mathrm{i}/2m_\mathrm{i})^{1/2}$, in order for the ion-acoustic wave not to be heavily Landau damped (1946). Fortunately, one of the major effects of collisions in the scenarios with a high-Z^* target is the inverse bremsstrahlung heating discussed in §3.3.1, which heats the electrons and creates favorable conditions for electrostatic shock formation.

The collisional interaction between multiple ion species greatly complicates the problem. Besides velocity diffusion, there would also be an advection term linked to the friction between the different ion species moving at different velocities through the shock. For this reason, the work in paper **C** is based on collisional, 1D PIC simulations, with various laser and plasma parameters; a circularly polarized laser pulse was used in order to reduce unwanted side effects from high-energy electron bunches. The results show a shock structure, shown in Fig. 3.4, which is similar to that of the semi-analytical model from paper **A**. There is also a clear proton reflection. Note that the ions in this case do cross the constant energy trajectories shown in Fig. 3.4, that is mostly due to the decaying shock speed and amplitude, which is not captured in the semi-analytical steady-state model; for a constant speed and amplitude shock, there would have to be a steady supply of energy to the shock, in order to counteract the energy lost to the reflected ions.

Intriguingly, while the simulations in paper **C** show clear proton reflection, as in Fig. 3.4, the results by Turrell, Sherlock & Rose (2015) were very different, in that they found that inter-species collisions to cause strong enough collisional friction between the protons and Cs ions to effectively cancel all ion reflection by the shock; the strong friction meant that the energy that would otherwise be transferred from the shock to the reflected ions is now converted to heat in the downstream ion
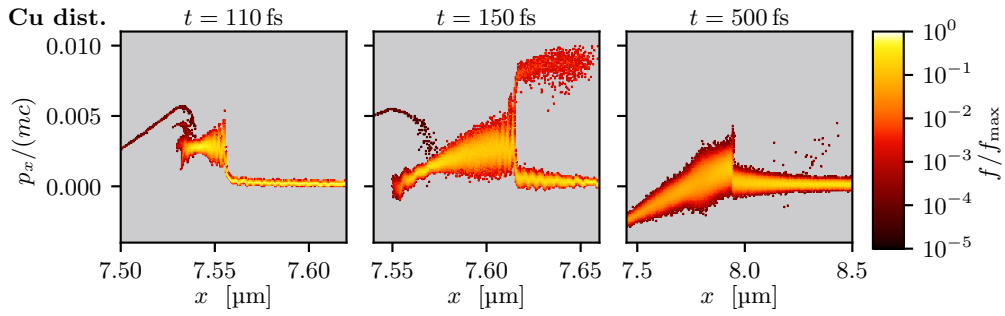
Figure 3.5: Illustration of the three stages of an electrostatic shock observed in copper targets in paper **C**: initial shock-like perturbation (at time $t = 110\,$fs), fully developed ion-reflecting shock ($t = 150\,$fs) and transition to a shock-remnant blast wave ($t = 500\,$fs).

populations. This discrepancy, despite using virtually identical physical parameters, is thought to be due to variations in the collisional algorithms for the PIC codes; further elaboration on this discussion can be found in paper **C**. This difference in outcome may be useful to experimentally verify either collision models.

Collisional self-amplifying ion reflection

Another issue on this topic is how the electrostatic shocks are formed in laser-driven plasmas. In high-intensity laser–plasma interactions, ion reflection can arise either from the so called "laser piston" in the radiation pressure acceleration (RPA) regime in overdense plasmas, due to the ponderomotive force (Silva *et al.*, 2004), or from electron pressure gradients in near-critical-density plasmas, which drive the expansion of the plasma out from the high-pressure region (Fiuza *et al.*, 2012). In the former, which is also closer to the scenarios studied in paper **C**, the velocity of the laser piston, $v_{\text{piston}} \simeq ca_0[Z^* m_e n_c/(m_i n_e)]^{1/2}$, determines the velocity of the shock.

In paper **C**, a new effect in connection with shock-reflection initialization is presented, based on collisional heating of the upstream ion population. As discussed in §3.4.1, ion-reflection is a fundamentally kinetic effect, where the reflected ions come from the high-energy tail of the upstream ion population (except perhaps in multi-ion-species cases involving hydrogen). So in order for ion reflection to occur, the upstream ion distributions must have a sufficient thermal width. What we found in paper **C**, is that collisions between ions in the reflected and incoming upstream populations lead to heating of these ions; and by heating up the incoming ion population, more ions will be reflected, which can further strengthen the collisional ion heating in the upstream. Collisions can therefore act to create an early self-amplification of shock ion reflection – especially in high-Z^* materials.

While this self-amplifying ion reflection has little discernible impact on the shock formation in the CsH target, since the protons are so easily reflected from the beginning, we found that it can contribute to the onset of ion-reflection in single-ion-species targets – especially for heavier ions. In the case of CsH targets, the laser-piston is strong enough to rapidly accelerate the protons, the starting point from which the electrostatic shock forms. In the pure Cu target, by contrast, the

laser pulse induces a shock-like perturbation, which outruns the laser piston but initially does not reflect any ions, as shown in the $t = 110$ fs panel of Fig. 3.5. Initial upstream ion heating, through electron–ion heat transfer, then initialized ion reflection, which self-amplifies to a fully developed, ion-reflecting, electrostatic shock, as shown in the $t = 150$ fs panel of Fig. 3.5.

As the shock progresses, and a larger and larger fraction of the upstream ions are reflected, the shock wave loses its energy to ion reflection. Finally the amplitude and speed of the shock is no longer able to sustain ion reflection and the shock subsides and transitions into a blast wave – a supersonic remnant of the original shock. This is shown in the $t = 500$ fs panel of Fig. 3.5. The remaining blast wave is now traveling through the upstream ion population which has been heated by collisional stopping of the reflected ions, and the blast wave itself further heats up the ions as they pass into the downstream.

Chapter 4

Summary and outlook

In the previous chapters, the focus has been on the background physics, while making a number of observations with regards to the work done in the papers included in this thesis. In this chapter, we will briefly summarize the content of the papers and give an outlook of possible directions of future research on the topic.

4.1 Summary of papers

The common theme of the papers has been to study collisional effects in laser-plasma settings – laser-plasma heating and electrostatic shocks. In other studies of these settings, the role of collisions is sometimes justifiably neglected and sometimes overlooked. The studies have all been performed in the kinetic framework, either as a direct semi-analytical kinetic model (paper **A**) or through the use of particle-in-cell simulations (paper **B** and **C**). Paper **A** treats collisional effects in weakly collisional plasmas, whereas papers **B** and **C** study the effects of collisions in cases where the plasma has been specifically chosen to be as collisional as possible given the circumstances.

In paper A, we expand upon a semi-analytical model from Cairns *et al.* (2014, 2015) and Pusztai *et al.* (2018), to include velocity diffusion due to ion–ion collisions in a single-ion-species plasma. The model is based upon a perturbative treatment in the smallness of the collisionality, $\nu\lambda_{\mathrm{D}}/c_{\mathrm{s}} \ll 1$, and is thus only suitable for electrostatic shocks in rather weakly collisional plasmas, such as space plasmas and perhaps low-density (gas-jet) laser-target plasmas.

The collisional velocity diffusion causes ions to enter regions of phase space where they become trapped due to the electrostatic potential oscillation in the shock downstream. The accumulation of ions in the trapped regions upsets the charge balance of the electrostatic shock, causing the downstream oscillations to grow. On the other hand, the height of the electrostatic potential barrier at the shock front remains essentially unchanged, and hence the shock-reflected fraction of incoming ions also remains essentially unchanged. The amplitude of the downstream oscillations are found to grow as $\sqrt{\nu t}$, where νt is dubbed the collisional age of the shock. Since shocks can be long-lived – especially in space plasmas – and the effect of the collisional diffusion is cumulative, collisions can become important for the shock

dynamics, even though the collisionality is very weak.

As a complement to the semi-analytical model, we also performed kinetic simulation using the Vlasov–Maxwell solver in the `Gkeyll` code framework. At the time, `Gkeyll` only had support for the Dougherty (or Lenard–Bernsein) operator, which does not have the same strong negative velocity dependence as the Fokker–Planck operator. The consequence was that the collisional coupling between populations separated by a large velocity difference became artificially strong, which quickly broke down the shock structure. These results show a cautionary example on the importance of choosing a collision operator suited for the situation being modeled.

In paper B, we revisit inverse bremsstrahlung as a possible energy-absorption mechanism for an ultraintense and ultrashort laser pulse hitting a solid copper target, using the `Smilei` (Derouillat *et al.*, 2018) particle-in-cell simulations. The electrons are heated to temperatures of several keV. By using a circularly polarized laser pulse, the number of high-energy electrons is reduced compared to linear polarization, which in turn leads to a faster thermalization of the electrons. The creation of well-thermalized, hot and dense plasmas is attractive for warm-dense-matter studies. From comparisons to simulations with collisions disabled, we find that inverse bremsstrahlung is responsible for most of the energy absorption.

A crucial element why collisions become important is the fact that the copper plasma was ionized to a relatively high level of $Z^* = 27$. To test this assumed ionization level, an additional simulation was performed, where the ionization of the individual macro-particle ions was self-consistently simulated, using both collisional impact ionization and field ionization. In this simulation, the laser field quickly ionizes the skin-layer ions to $Z^* \gtrsim 20$, and collisional impact ionization then gradually brings up the ionization level to $Z^* \simeq 27$ in the whole plasma, which justifies the assumed $Z^* = 27$ in the other simulations. Importantly, since the ionization quickly reaches relatively high levels in the skin region, where the absorption happens, the absorbed energy becomes comparable to that of the fixed-ionization simulation.

Due to field ionization in the charge-separation layer, some electrons were freed already inside effectively the "vacuum region", outside the electron boundary of the plasma. These electrons, injected into a region of strong laser field, were accelerated to high energies similar to the vacuum heating mechanism with LP. The electron energy spectrum of the self-consistently ionized target plasma, was subsequently less thermalized than the fixed-ionization counterpart.

Collisional absorption was also studied with respect to variations in the laser parameters through a wide scan in laser intensity and pulse duration. A power-law scaling is found, and the absorption efficiency is found to scale as (pulse amplitude)$^{-0.52}\times$ (pulse duration)$^{0.13}$. Therefore, at fixed laser pulse energy, increasing the pulse duration rather than the intensity leads to a higher electron temperature. Furthermore, the collisional absorption was also tested against transverse plasma instabilities by performing a two-dimensional simulation, which showed very similar behavior as its one-dimensional counterpart.

As a demonstration of the inverse bremsstrahlung mechanism, we also performed simulations with a simplified setup, with frozen ions in a semi-infinite plasma and a fixed (after a short ramp-up) intensity laser. This setup is meant to generate

a quasi-steady-state laser-plasma, where the mechanism by which collisions cause absorption can be isolated and investigated in isolation, apart from, e.g., effects of intensity modulation or hot electron recirculation. Neglecting the ion motion, one can assume that laser absorption only results from the (density of) power absorbed by the electrons moving in the transverse laser electric field, $-en_e \boldsymbol{E}_\perp \cdot \boldsymbol{v}_{e,\perp}$. In a collisionless plasma, conservation of transverse canonical momentum implies that $\boldsymbol{v}_{e,\perp}$ and $\boldsymbol{E}_\perp$ are perpendicular to each other and thus result in no net energy transfer. However, collisions break the conservation of transverse canonical momentum for the electrons (by transferring momentum to the ions) and cause a small shift in $\boldsymbol{v}_{e,\perp}$, both in magnitude and phase angle, with respect to $\boldsymbol{E}_\perp$, which in turn cause a net energy transfer from the laser to the electrons. This setup may provide a good framework for analytical investigation of the scaling laws observed in the laser-parameter scan.

In paper C, we investigate the impact of collisions on the ion dynamics in solid density caesium hydride and copper targets irradiated by high-intensity and ultrashort-duration circularly polarized laser pulses. As in paper **B**, the study was performed using particle-in-cell simulations employing the Smilei PIC code (Derouillat *et al.*, 2018). Since both target materials have a relatively high Z^*, collisions significantly enhance the electron heating, as discussed in paper **B**, which creates more favorable conditions for shock formation. In comparison, simulations made without collisions show signs of a shock as well, although with much lower speed and amplitude than the corresponding collisional simulations.

The results from the caesium hydride (CsH) target, are compared with previous work by Turrell, Sherlock & Rose (2015) and significant differences are found, despite simulating virtually identical setups[*]. The main difference is whether or not inter-species collisional friction would be sufficiently strong to cancel the shock ion reflection, which is what is observed in the simulations by Turrell, Sherlock & Rose (2015), while we do not observe such strong friction. We believe that this discrepancy is due to the two different collisional algorithms used in the Smilei (Derouillat *et al.*, 2018) and EPOCH (Arber *et al.*, 2015) PIC codes, employed by us and Turrell, Sherlock & Rose, respectively. The main idea is that the collisional algorithms are originally designed to emulate the Fokker–Planck operator in low-density or high-temperature plasmas, where the Fokker–Planck operator is valid, but the collisional behavior then has to be modified in high-density (or low-temperature) plasmas – which is the case for the CsH plasma at hand. This high-density/low-temperature modification differs between the two algorithms used. We believe that the collisional algorithm used by Smilei (Pérez *et al.*, 2012) has better physical grounds for its modification, and thus produce the more physically accurate results.

With copper targets, we find that the lack of embedded protons results in the launch of a shock-like perturbation which initially is not capable of reflecting ions. We conclude that collisions play an important role in promoting shock ion reflection, due to collisional heating between the reflected and incoming upstream ion populations. This self-amplification leads to the shock ion reflection bootstrapping itself.

---

[*]We even have simulations with *exactly* the same physical parameters, with the same difference being observed.
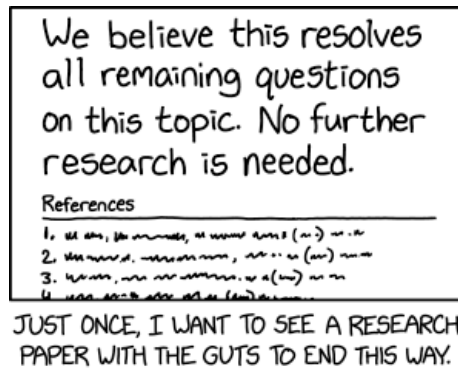
Figure 4.1: *"Further research is needed to understand how we managed to do such a good job."* – Randall Munroe (2020). Reproduced from `https://xkcd.com/2268/` © ① ⑤ 2.5

At later times, the energy lost by the shock to the increasing fraction of reflected ions results in a demise of the shock, which transforms into a hydrodynamic blast wave.

4.2 Outlook

While I would like to end this thesis as Randall Munroe (2020) wishes to see a research paper end (Fig. 4.1), there are several avenues of improvements and further research. A general area of research which needs more attention is a more comprehensive study of the effects of collisions over a broader range of collisionality, from the collisionless to the collision-dominated regime.

Beginning with the use of inverse bremsstrahlung for isochoric heating in paper **B**, one may express some concern about the still rather low efficiency of the collisional absorption, in the order of a couple of percent. The simulated targets were all of the same thickness, while one may expect that the target size may affect the results. For instance, thicker targets may require a longer time for the temperature to equilibrate. This complication could be considered with respect to practical warm/hot-dense-matter (W/HDM) applications, preferably in collaboration with experts in (x-ray) diagnostics of W/HDM in order to assess the impact of such effects. There would also be opportunities to study how the various absorption mechanisms affect the x-ray signatures of the created W/HDM.

As mentioned in the summary of this paper, the quasi-steady-state simulations make a good basis for a (semi-)analytical model of the inverse bremsstrahlung heating. The main goal of such a model would be to understand and explain the observed power-law scalings. This work would aim at understanding the kinetic dynamics of the electrons due to a spread in the transverse momentum plane of phase space, especially how that spread affects the longitudinal motion of the electrons. The analytical work could be complemented by a simplified numerical model that describes this dynamics.

In addressing ionization, we found that ionization injection of electrons into the vacuum region with strong laser fields impacts the thermalization of the plasma.

While this does not detract from the statement that CP produces a more thermalized plasma than LP – since the same ionization injection would happen with LP as well – this generation of high-energy electrons might be considered for other applications where such electrons are desirable. In general, the effect and dynamics of field ionization as a fast electron source has received little research attention and could be studied more thoroughly, not only in the context of laser absorption.

There are other effects which were not studied in paper **B**, such as the influence of a preplasma. The laser–plasma interaction can change quite drastically depending on the plasma-density profile at the target front surface. It would therefore be valuable to study the sensitivity of inverse bremsstrahlung heating with respect to the preplasma size – both in terms of energy-absorption efficiency and how it affects the thermalization of the electrons. Preliminary simulations indicate that the absorption efficiency is negatively affected by including a preplasma for circularly polarized lases pulses, but a more detailed investigation is needed.

One possibility to further broaden the study of inverse bremsstrahlung heating in paper **B** would be to investigate how higher-dimensional effects might affect the heating. A two-dimensional test was performed and presented in the paper, which suggested that the heating is not sensitive to transverse instabilities. However, since the ponderomotive force (3.29) depends on the gradient of the intensity, ∇I, a study of the effects of a spatial intensity envelope would also be valuable. Ideally, simulations should be made at larger scales, which would provide insights into how the problem scales with the size and dimensionality of the plasma. However, due to the high numerical resolution required to accurately model collisions, such large-scale and high-dimensional simulations are prohibitively computationally expensive at the moment.

From a broader perspective, the collisional heating could be studied in combination with more exotic targets. For example, only using a thin layer of high-Z^* material to provide electron heating, and then combining it with another material optimized for other purposes, such as to produce electrostatic shocks. Since electrostatic shocks require a high electron temperature, but also more preferably accelerate protons, the heating from a thin (tens of manometers) copper target could perhaps be combined with a plastic target in order to generate a stronger (proton-accelerating) shock than either of the target materials on their own.

Continuing with the semi-analytical studies of electrostatic shocks in paper **A**. The semi-analytical model as a whole (not just the collisional diffusion), is a steady-state model, with pure shock parameters (e.g. Mach number) as inputs to the model; it would therefore be interesting if the model could be expanded to "real world" inputs, such as for instance laser parameters. Yet, as seen when comparing the model, as it stands now, with shocks from simulations (e.g., figures 3.3 and 3.4, respectively), the semi-analytical model may still be used to constrain the local structure of a shock in more complex settings. However, that remains to be investigated further.

While the study of velocity diffusion leads to some more general conclusions about the effects of collisions on the shocks, our description is restricted to one type of collisions, and only in a limited region of phase space. There is still room for further analytical developments, such as multi-species collisions or considering the

effects of collisional friction between the incoming and reflected ions, especially with respect to the observations of self-amplifying ion reflection made in paper **C**. Both cases would require improving the model to capture the effect of a varying collision frequency. The latter case would furthermore require an refinement with a velocity dependent collision frequency; the effects of which could also be studied with respect to the diffusion and trapping in the downstream region.

Another question related to the ions orbiting in the boundary layer of the trapped region, is whether or not these counter-streaming ion populations may excite some instability, such as electron–ion or ion–ion acoustic instabilities (Gary, 1993). Perhaps there are some parameter regimes which are more susceptible to such instabilities. These instabilities can either be investigated analytically, or via simulations initialized with a shock distribution calculated from the semi-analytical model.

Simulations could also be used to study the long-time limit of collisional effects, beyond the reach of the perturbative approach in paper **A**, or the impact of other aspects of collisions, e.g. friction. However, as already noted, the simulated collision operator needs to have a sufficiently strong velocity dependent collision frequency – ideally it should be a full Fokker–Planck operator – in order to properly model the collisional interaction of velocity-separated populations.

Finally, we consider the simulation study in paper **C** of the collisional effects on the ion and shock dynamics. Like with paper **B**, further studies on the sensitivity of the problem to its dimensionality would be valuable. Electrostatic shocks are indeed expected to be highly sensitive to transverse non-uniformities, in particular due to the development of the strongly oblique ion–ion instability (Dieckmann *et al.*, 2013). Thanks to the similarities, the simulations required can likely be shared with the those required to study higher-dimensional effects to the inverse bremsstrahlung heating.

It would be interesting to study the effects of collisions in a slightly weaker collisionality regime, such as lower-charge materials. In fact, from a scan in Z^* (artificially chosen at four fixed values) performed for paper **B**, we can find qualitatively different shock behaviors likely due to variations in the plasma collisionality with Z^*. A closer examination throughout the range of collisionality could shed light on the plasma conditions for which collisions can be neglected in shock studies. In addition, one could investigate the impact of the laser parameters and the plasma density profile.

One interesting consideration with respect to the different results between paper **C** and by Turrell, Sherlock & Rose (2015), is that this difference could be used to experimentally verify the different collision algorithms, specifically their high-density/low-temperature corrections. Since our results differ in such a dramatic manner as to whether or not the shock is capable of accelerating ions, its may be possible to experimentally distinguish the two results from each other. By simulating laser-driven shocks in multi-species plasmas using different algorithms, the proton energy spectra obtained numerically could be compared to ditto of an experiment. In doing so, however, care will be needed to suppress, or experimentally differentiate, other ion acceleration mechanisms.

References

AMIRANOFF, F., BATON, S., BERNARD, D., CROS, B., DESCAMPS, D., DORCHIES, F., JACQUET, F., MALKA, V., MARQUÈS, J. R., MATTHIEUSSENT, G., MINÉ, P., MODENA, A., MORA, P., MORILLO, J. & NAJMUDIN, Z. 1998 "Observation of laser wakefield acceleration of electrons". *Phys. Rev. Lett.* **81**, 995–998, DOI: 10.1103/PhysRevLett.81.995

ANTICI, P., BOELLA, E., CHEN, S. N., ANDREWS, D. S., BARBERIO, M., BÖKER, J., CARDELLI, F., FEUGEAS, J. L., GLESSER, M., NICOLAÏ, P., ROMAGNANI, L., SCISCIÒ, M., STARODUBTSEV, M., WILLI, O., KIEFFER, J. C., TIKHONCHUK, V., PÉPIN, H., SILVA, L. O., D'HUMIÈRES, E. & FUCHS, J. 2017 "Acceleration of collimated 45 mev protons by collisionless shocks driven in low-density, large-scale gradient plasmas by a 10^{20} w/cm^2, 1 μm laser". *Scientific Reports* **7** (1), 1–9, DOI: 10.1038/s41598-017-15449-8

ARBER, T. D., BENNETT, K., BRADY, C. S., LAWRENCE-DOUGLAS, A., RAMSAY, M. G., SIRCOMBE, N. J., GILLIES, P., EVANS, R. G., SCHMITZ, H., BELL, A. R. & RIDGERS, C. P. 2015 "Contemporary particle-in-cell approach to laser-plasma modelling". *Plasma Physics and Controlled Fusion* **57** (11), 113 001, DOI: 10.1088/0741-3335/57/11/113001

BAILEY, J. E., ROCHAU, G. A., IGLESIAS, C. A., ABDALLAH, J., MACFARLANE, J. J., GOLOVKIN, I., WANG, P., MANCINI, R. C., LAKE, P. W., MOORE, T. C., BUMP, M., GARCIA, O. & MAZEVET, S. 2007 "Iron-plasma transmission measurements at temperatures above 150 eV". *Phys. Rev. Lett.* **99**, 265 002, DOI: 10.1103/PhysRevLett.99.265002

BARGSTEN, C., HOLLINGER, R., CAPELUTO, M. G., KAYMAK, V., PUKHOV, A., WANG, S., ROCKWOOD, A., WANG, Y., KEISS, D., TOMMASINI, R., LONDON, R., PARK, J., BUSQUET, M., KLAPISCH, M., SHLYAPTSEV, V. N. & ROCCA, J. J. 2017 "Energy penetration into arrays of aligned nanowires irradiated with relativistic intensities: Scaling to terabar pressures". *Sci. Adv.* **3**, e1601 558, DOI: 10.1126/sciadv.1601558

BAUER, D. & MULSER, P. 2007 "Vacuum heating versus skin layer absorption of intense femtosecond laser pulses". *Physics of Plasmas* **14** (2), 023 301, DOI: 10.1063/1.2435326

BELIAEV, S. T. & BUDKER, G. I. 1956 "The relativistic kinetic equation". *Soviet Physics Doklady* **1**, 218

BELL, A. R. & KINGHAM, R. J. 2003 "Resistive collimation of electron beams in laser-produced plasmas". *Phys. Rev. Lett.* **91**, 035 003, DOI: 10.1103/PhysRevLett.91.035003

BENDER, P. L. *et al.* 1973 "The Lunar Laser Ranging Experiment: Accurate ranges have given a large improvement in the lunar orbit and new selenophysical information". *Science* **182** (4109), 229–238, DOI: 10.1126/science.182.4109.229

BHATNAGAR, P. L., GROSS, E. P. & KROOK, M. 1954 "A model for collision processes in gases. I. small amplitude processes in charged and neutral one-component systems". *Phys. Rev.* **94**, 511–525, DOI: 10.1103/PhysRev.94.511

BOGOLJUBOV, N. N. 1960 Problems of a dynamical theory in statistical physics. Geophysics Research Directorate, AF Cambridge Research Laboratories, Air Force Research Division, United States

BOLTZMANN, L. 1872 "Weitere Studien über das Wärmegleichgewicht unter Gasmolekülen (Eng. Further studies on the thermal equilibrium of gas molecules)". *Sitzungsberichte der Kaiserlichen Akademie der Wissenschaften* **66**, 275–370. An English translation can be found at DOI: 10.1142/9781848161337_0015.

BORGHESI, M., CAMPBELL, D. H., SCHIAVI, A., HAINES, M. G., WILLI, O., MACKINNON,

A. J., Patel, P., Gizzi, L. A., Galimberti, M., Clarke, R. J., Pegoraro, F., Ruhl, H. & Bulanov, S. 2002 "Electric field detection in laser-plasma interaction experiments via the proton imaging technique". *Physics of Plasmas* **9** (5), 2214–2220, doi: 10.1063/1.1459457

Boris, J. P. 1970 "Relativistic plasma simulation-optimization of a hybrid code". In "Proceedings, Fourth Conference on Numerical Simulation of Plsms", (3–8)

Born, M. & Green, H. 1946 "A general kinetic theory of liquids I. The molecular distribution functions". *Proceedings of the Royal Society of London. Series A.* **188** (1012), 10–18, doi: 10.1098/rspa.1946.0093

Braams, B. J. & Karney, C. F. F. 1987 "Differential form of the collision integral for a relativistic plasma". *Phys. Rev. Lett.* **59**, 1817–1820, doi: 10.1103/PhysRevLett.59.1817

Brown, C. R. D., Hoarty, D. J., James, S. F., Swatton, D., Hughes, S. J., Morton, J. W., Guymer, T. M., Hill, M. P., Chapman, D. A., Andrew, J. E., Comley, A. J., Shepherd, R., Dunn, J., Chen, H., Schneider, M., Brown, G., Beiersdorfer, P. & Emig, J. 2011 "Measurements of electron transport in foils irradiated with a picosecond time scale laser pulse". *Phys. Rev. Lett.* **106**, 185 003, doi: 10.1103/PhysRevLett.106.185003

Brunel, F. 1987 "Not-so-resonant, resonant absorption". *Phys. Rev. Lett.* **59**, 52–55, doi: 10.1103/PhysRevLett.59.52

Bulanov, S. V., Esirkepov, T. Zh., Khoroshkov, V. S., Kuznetsov, A. V. & Pegoraro, F. 2002 "Oncological hadrontherapy with laser ion accelerators". *Physics Letters A* **299** (2), 240 – 247, doi: 10.1016/S0375-9601(02)00521-2

Cagas, P., Hakim, A., Scales, W. & Srinivasan, B. 2017 "Nonlinear saturation of the weibel instability". *Physics of Plasmas* **24** (11), 112 116, doi: 10.1063/1.4994682

Cairns, R. A., Bingham, R., Norreys, P. & Trines, R. G. M. 2014 "Laminar shocks in high power laser plasma interactions". *Physics of Plasmas* **21** (2), 022 112, doi: 10.1063/1.4864328

Cairns, R. A., Bingham, R., Trines, R. G. M. & Norreys, P. 2015 "Weak collisionless shocks in laser-plasmas". *Plasma Physics and Controlled Fusion* **57** (4), 044 008, doi: 10.1088/0741-3335/57/4/044008

Catto, P. J. & More, R. M. 1977 "Sheath inverse bremsstrahlung in laser produced plasmas". *The Physics of Fluids* **20** (4), 704–705, doi: 10.1063/1.861930

Chen, S. N., Gregori, G., Patel, P. K., Chung, H.-K., Evans, R. G., Freeman, R. R., Garcia Saiz, E., Glenzer, S. H., Hansen, S. B., Khattak, F. Y., King, J. A., Mackinnon, A. J., Notley, M. M., Pasley, J. R., Riley, D., Stephens, R. B., Weber, R. L., Wilks, S. C. & Beg, F. N. 2007 "Creation of hot dense matter in short-pulse laser-plasma interaction with tamped titanium foils". *Physics of Plasmas* **14** (10), 102 701, doi: 10.1063/1.2777118

Daido, H., Nishiuchi, M. & Pirozhkov, A. S. 2012 "Review of laser-driven ion sources and their applications". *Reports on progress in physics* **75** (5), 056 401, doi: 10.1088/0034-4885/75/5/056401

Denavit, J. 1992 "Absorption of high-intensity subpicosecond lasers on solid density targets". *Phys. Rev. Lett.* **69**, 3052–3055, doi: 10.1103/PhysRevLett.69.3052

Derouillat, J., Beck, A., Pérez, F., Vinci, T., Chiaramello, M., Grassi, A., Flé, M., Bouchard, G., Plotnikov, I., Aunai, N., Dargent, J., Riconda, C. & Grech, M. 2018 "Smilei: A collaborative, open-source, multi-purpose particle-in-cell code for plasma simulation". *Comput. Phys. Commun.* **222**, 351, doi: 10.1016/j.cpc.2017.09.024

Dervieux, V., Loupias, B., Baton, S., Lecherbourg, L., Glize, K., Rousseaux, C., Reverdin, C., Gremillet, L., Blancard, C., Silvert, V., Pain, J.-C., Brown, C. R. D., Allan, P., Hill, M. P., Hoarty, D. J. & Renaudin, P. 2015 "Characterization of near-LTE, high-temperature and high-density aluminum plasmas produced by ultra-high intensity lasers". *High Energy Density Physics* **16**, 12 – 17, doi: 10.1016/j.hedp.2015.04.009

Dieckmann, M. E., Sarri, G., Doria, D., Pohl, M. & Borghesi, M. 2013 "Modification of the formation of high-Mach number electrostatic shock-like structures by the ion acoustic

instability". *Physics of Plasmas* **20** (10), 102 112, DOI: `10.1063/1.4825339`

DIECKMANN, M. E., DORIA, D., SARRI, G., ROMAGNANI, L., AHMED, H., FOLINI, D., WALDER, R., BRET, A. & BORGHESI, M. 2017 "Electrostatic shock waves in the laboratory and astrophysics: similarities and differences". *Plasma Physics and Controlled Fusion* **60** (1), 014 014, DOI: `10.1088/1361-6587/aa8c8f`

DOUGHERTY, J. P. 1964 "Model Fokker–Planck equation for a plasma and its solution". *The Physics of Fluids* **7** (11), 1788–1799, DOI: `10.1063/1.2746779`

DOUGHERTY, J. P. & WATSON, S. R. 1967 "Model Fokker–Planck equations: Part 2. The equation for a multicomponent plasma". *Journal of Plasma Physics* **1** (3), 317–326, DOI: `10.1017/S0022377800003329`

DRAKE, R. P. 2018 "A journey through high-energy-density physics". *Nuclear Fusion* **59** (3), 035 001, DOI: `10.1088/1741-4326/aaf0e3`

DYER, G. M., BERNSTEIN, A. C., CHO, B. I., OSTERHOLZ, J., GRIGSBY, W., DALTON, A., SHEPHERD, R., PING, Y., CHEN, H., WIDMANN, K. & DITMIRE, T. 2008 "Equation-of-state measurement of dense plasmas heated with fast protons". *Phys. Rev. Lett.* **101**, 015 002, DOI: `10.1103/PhysRevLett.101.015002`

ESIRKEPOV, T., BORGHESI, M., BULANOV, S. V., MOUROU, G. & TAJIMA, T. 2004 "Highly efficient relativistic-ion generation in the laser-piston regime". *Phys. Rev. Lett.* **92**, 175 003, DOI: `10.1103/PhysRevLett.92.175003`

EVANS, R. G., CLARK, E. L., EAGLETON, R. T., DUNNE, A. M., EDWARDS, R. D., GARBETT, W. J., GOLDSACK, T. J., JAMES, S., SMITH, C. C., THOMAS, B. R., CLARKE, R., NEELY, D. J. & ROSE, S. J. 2005 "Rapid heating of solid density material by a petawatt laser". *Applied Physics Letters* **86** (19), 191 505, DOI: `10.1063/1.1920422`

FAURE, J., GLINEC, Y., PUKHOV, A., KISELEV, S., GORDIENKO, S., LEFEBVRE, E., ROUSSEAU, J.-P., BURGY, F. & MALKA, V. 2004 "A laser–plasma accelerator producing monoenergetic electron beams". *Nature* **431** (7008), 541–544, DOI: `10.1038/nature02963`

FAUSSURIER, G. & BLANCARD, C. 2019 "Pressure in warm and hot dense matter using the average-atom model". *Phys. Rev. E* **99**, 053 201, DOI: `10.1103/PhysRevE.99.053201`

FEWS, A. P., NORREYS, P. A., BEG, F. N., BELL, A. R., DANGOR, A. E., DANSON, C. N., LEE, P. & ROSE, S. J. 1994 "Plasma ion emission from high intensity picosecond laser pulse interactions with solid targets". *Phys. Rev. Lett.* **73**, 1801–1804, DOI: `10.1103/PhysRevLett.73.1801`

FIUZA, F., STOCKEM, A., BOELLA, E., FONSECA, R. A., SILVA, L. O., HABERBERGER, D., TOCHITSKY, S., GONG, C., MORI, W. B. & JOSHI, C. 2012 "Laser-driven shock acceleration of monoenergetic ion beams". *Phys. Rev. Lett.* **109**, 215 001, DOI: `10.1103/PhysRevLett.109.215001`

FIUZA, F., SWADLING, G. F., GRASSI, A., RINDERKNECHT, H. G., HIGGINSON, D. P., RYUTOV, D. D., BRUULSEMA, C., DRAKE, R. P., FUNK, S., GLENZER, S., GREGORI, G., LI, C. K., POLLOCK, B. B., REMINGTON, B. A., ROSS, J. S., ROZMUS, W., SAKAWA, Y., SPITKOVSKY, A., WILKS, S. & PARK, H.-S. 2020 "Electron acceleration in laboratory-produced turbulent collisionless shocks". *Nature Physics* (1–5), DOI: `10.1038/s41567-020-0919-4`

FORSLUND, D. W. & SHONK, C. R. 1970 "Formation and structure of electrostatic collisionless shocks". *Phys. Rev. Lett.* **25**, 1699, DOI: `10.1103/PhysRevLett.25.1699`

FUJIOKA, S., TAKABE, H., YAMAMOTO, N., SALZMANN, D., WANG, F., NISHIMURA, H., LI, Y., DONG, Q., WANG, S., ZHANG, Y., RHEE, Y.-J., LEE, Y.-W., HAN, J.-M., TANABE, M., FUJIWARA, T., NAKABAYASHI, Y., ZHAO, G., ZHANG, J. & MIMA, K. 2009 "X-ray astronomy in the laboratory with a miniature compact object produced by laser-driven implosion". *Nat. Phys.* **8**, 821, DOI: `10.1038/NPHYS1402`

GARY, S. P. 1993 Theory of Space Plasma Microinstabilities. Cambridge Atmospheric and Space Science Series, Cambridge University Press, DOI: `10.1017/CBO9780511551512`

GIBBON, P. 2005 Short Pulse Laser Interactions with Matter. London: Imperial College Press, DOI: `10.1142/p116`

References

Gitomer, S. J., Jones, R. D., Begay, F., Ehler, A. W., Kephart, J. F. & Kristal, R. 1986 "Fast ions and hot electrons in the laser–plasma interaction". *The Physics of Fluids* **29** (8), 2679–2688, doi: 10.1063/1.865510

Giulietti, A. & Tajima, T. 2016 "Lasers Offer New Tools to Radiobiology and Radiotherapy". In "Laser-Driven Particle Acceleration Towards Radiobiology and Medicine", (ed. A. Giulietti), Biological and Medical Physics, Biomedical Engineering, Springer International Publishing, ISBN 978-3-319-31563-8, doi: 10.1007/978-3-319-31563-8_1

Green, H. S. 1952 The molecular theory of fluids. North-Holland

Gregori, G., Hansen, S. B., Clarke, R., Heathcote, R., Key, M. H., King, J., Klein, R. I., Izumi, N., Mackinnon, A. J., Moon, S. J., Park, H.-S., Pasley, J., Patel, N., Patel, P. K., Remington, B. A., Ryutov, D. D., Shepherd, R., Snavely, R. A., Wilks, S. C., Zhang, B. B. & Glenzer, S. H. 2005 "Experimental characterization of a strongly coupled solid density plasma generated in a short-pulse laser target interaction". *Contributions to Plasma Physics* **45** (3-4), 284–292, doi: 10.1002/ctpp.200510032

Guillory, J. & Benford, G. 1972 "Estimates of dense plasma heating by stable intense electron beams". *Plasma Physics* **14** (12), 1131–1138, doi: 10.1088/0032-1028/14/12/007

Haberberger, D., Tochitsky, S., Fiuza, F., Gong, C., Fonseca, R. A., Silva, L. O., Mori, W. B. & Joshi, C. 2012 "Collisionless shocks in laser-produced plasma generate monoenergetic high-energy proton beams". *Nat. Phys.* **8**, 95–99, doi: 10.1038/nphys2130

Hakim, A., Francisquez, M., Juno, J. & Hammett, G. W. 2020 "Conservative discontinuous Galerkin schemes for nonlinear Dougherty–Fokker–Planck collision operators". *Journal of Plasma Physics* **86** (4), 905860 403, doi: 10.1017/S0022377820000586

Helander, P. & Sigmar, D. J. 2002 Collisional Transport in Magnetized Plasmas, vol. 4 of *Cambridge Monographs on Plasma Physics*. Cambridge University Press, ISBN 978-0-521-02098-5

Higginson, A., Gray, R. J., King, M., Dance, R. J., Williamson, S. D. R., Butler, N. M. H., Wilson, R., Capdessus, R., Armstrong, C., Green, J. S., Hawkes, J., Martin, P., Wei, W. Q., Mirfayzi, S. R., Yuan, X. H., Kar, S., Borghesi, M., Clarke, R. J., Neely, D. & McKenna, P. 2018 "Near-100 MeV protons via a laser-driven transparency-enhanced hybrid acceleration scheme". *Nat. Commun.* **9** (1), 724, doi: 10.1038/s41467-018-03063-9

Hoarty, D. J., Allan, P., James, S. F., Brown, C. R. D., Hobbs, L. M. R., Hill, M. P., Harris, J. W. O., Morton, J., Brookes, M. G., Shepherd, R., Dunn, J., Chen, H., von Marley, E., Beiersdorfer, P., Chung, H. K., Lee, R. W., Brown, G. & Emig, J. 2013a "Observations of the effect of ionization-potential depression in hot dense plasma". *Phys. Rev. Lett.* **110**, 265 003, doi: 10.1103/PhysRevLett.110.265003

Hoarty, D. J., Allan, P., James, S. F., Brown, C. R. D., Hobbs, L. M. R., Hill, M. P., Harris, J. W. O., Morton, J., Brookes, M. G., Shepherd, R., Dunn, J., Chen, H., von Marley, E., Beiersdorfer, P., Chung, H. K., Lee, R. W., Brown, G. & Emig, J. 2013b "The first data from the Orion laser; measurements of the spectrum of hot, dense aluminium". *High Energy Density Physics* **9** (4), 661 – 671, doi: 10.1016/j.hedp.2013.06.005

Jackson, J. D. 1999 Classical Electrodynamics. 3rd edn., Wiley, ISBN 978-0-471-30932-1

Joshi, C., Mori, W. B., Katsouleas, T., Dawson, J. M., Kindel, J. M. & Forslund, D. W. 1984 "Ultrahigh gradient particle acceleration by intense laser-driven plasma density waves". *Nature* **311** (5986), 525–529, doi: 10.1038/311525a0

Juno, J. 2020 "A deep dive into the distribution function: Understanding phase space dynamics with continuum vlasov-maxwell simulations". Ph.D. thesis, University of Maryland, College Park, Maryland. https://arxiv.org/abs/2005.13539

Juno, J., Hakim, A., TenBarge, J., Shi, E. & Dorland, W. 2018 "Discontinuous galerkin algorithms for fully kinetic plasmas". *Journal of Computational Physics* **353**, 110 – 147, doi: 10.1016/j.jcp.2017.10.009

Jüttner, F. 1911 "Das Maxwellsche Gesetz der Geschwindigkeitsverteilung in der Relativtheorie".

Annalen der Physik **339** (5), 856–882, DOI: 10.1002/andp.19113390503. In German, English title roughly "The Maxwellian law of the velocity distribution in the theory of relatvity".

KAW, P. & DAWSON, J. 1970 "Relativistic nonlinear propagation of laser beams in cold overdense plasmas". *The Physics of Fluids* **13** (2), 472–481, DOI: 10.1063/1.1692942

KEENAN, B. D., SIMAKOV, A. N., TAITANO, W. T. & CHACÓN, L. 2018 "Ion species stratification within strong shocks in two-ion plasmas". *Physics of Plasmas* **25** (3), 032 103, DOI: 10.1063/1.5020156

KIM, I. J., PAE, K. H., CHOI, I. W., LEE, C.-L., KIM, H. T., SINGHAL, H., SUNG, J. H., LEE, S. K., LEE, H. W., NICKLES, P. V., JEONG, T. M., KIM, C. M. & NAM, C. H. 2016 "Radiation pressure acceleration of protons to 93 mev with circularly polarized petawatt laser pulses". *Physics of Plasmas* **23** (7), 070 701, DOI: 10.1063/1.4958654

KIRKWOOD, J. G. 1946 "The statistical mechanical theory of transport processes I. General theory". *The Journal of Chemical Physics* **14** (3), 180–201, DOI: 10.1063/1.1724117

KLIMONTOVICH, YU. L. 1967 The Statistical Theory of Non-Equilibrium Processes in a Plasma, vol. 9 of *International Series in Natural Philosophy*. Pergamon, ISBN 978-0-08-011966-3, DOI: 10.1016/C2013-0-06978-2

KNUDSON, M. D., DESJARLAIS, M. P. & DOLAN, D. H. 2008 "Shock-wave exploration of the high-pressure phases of carbon". *Science* **322** (5909), 1822–1825, DOI: 10.1126/science.1165278

KRUER, W. L. & ESTABROOK, K. 1985 "J×B heating by very intense laser light". *The Phys. of Fluids* **28**, 430–432, DOI: 10.1063/1.865171

LANDAU, L. D. 1946 "On the vibrations of the electronic plasma". *Zh. Eksp. Teor. Fiz.* **10**, 25, DOI: 10.1016/B978-0-08-010586-4.50066-3

LE PAPE, S. *et al.* 2018 "Fusion energy output greater than the kinetic energy of an imploding shell at the national ignition facility". *Phys. Rev. Lett.* **120**, 245 003, DOI: 10.1103/PhysRevLett.120.245003

LEBEDEW, P. 1901 "Untersuchungen über die Druckkräfte des Lichtes". *Annalen der Physik* **311** (11), 433–458, DOI: 10.1002/andp.19013111102. In German, English title roughly "Investigation of the pressure-force of light".

LEE, M. A., MEWALDT, R. A. & GIACALONE, J. 2012 "Shock acceleration of ions in the heliosphere". *Space science reviews* **173** (1-4), 247–281, DOI: 10.1007/s11214-012-9932-y

LENARD, A. & BERNSTEIN, I. B. 1958 "Plasma oscillations with diffusion in velocity space". *Phys. Rev.* **112**, 1456–1459, DOI: 10.1103/PhysRev.112.1456, URL https://link.aps.org/doi/10.1103/PhysRev.112.1456

LINLOR, W. I. 1963 "Ion energies produced by laser giant pulse". *Applied Physics Letters* **3** (11), 210–211, DOI: 10.1063/1.1753852

LINZ, U. & ALONSO, J. 2007 "What will it take for laser driven proton accelerators to be applied to tumor therapy?" *Phys. Rev. ST Accel. Beams* **10**, 094 801, DOI: 10.1103/PhysRevSTAB.10.094801

LITOS, M., ADLI, E., AN, W., CLARKE, C. I., CLAYTON, C. E., CORDE, S., DELAHAYE, J. P., ENGLAND, R. J., FISHER, A. S., FREDERICO, J., GESSNER, S., GREEN, S. Z., HOGAN, M. J., JOSHI, C., LU, W., MARSH, K. A., MORI, W. B., MUGGLI, P., VAFAEI-NAJAFABADI, N., WALZ, D., WHITE, G., WU, Z., YAKIMENKO, V. & YOCKY, G. 2014 "High-efficiency acceleration of an electron beam in a plasma wakefield accelerator". *Nature* **515** (7525), 92–95, DOI: 10.1038/nature13882

LORENZ, L. V. 1867 "Xxxviii. on the identity of the vibrations of light with electrical currents". *The London, Edinburgh, and Dublin Philosophical Magazine and Journal of Science* **34** (230), 287–301, DOI: 10.1080/14786446708639882

LOVELACE, R. V. & SUDAN, R. N. 1971 "Plasma heating by high-current relativistic electron beams". *Phys. Rev. Lett.* **27**, 1256–1259, DOI: 10.1103/PhysRevLett.27.1256

MACCHI, A. 2013 A Superintense Laser–Plasma Interaction Theory Primer. 1st edn., Springer, ISBN 978-94-007-6124-7

References

Macchi, A. 2014 "Theory of light sail acceleration by intense lasers: an overview". *High Power Laser Science and Engineering* **2**, e10, doi: 10.1017/hpl.2014.13

Macchi, A., Borghesi, M. & Passoni, M. 2013 "Ion acceleration by superintense laser-plasma interaction". *Rev. Mod. Phys.* **85**, 751–793, doi: 10.1103/RevModPhys.85.751

Maiman, T. H. 1960 "Stimulated optical radiation in ruby". *Nature* **187** (4736), 493–494, doi: 10.1038/187493a0

Mančić, A., Lévy, A., Harmand, M., Nakatsutsumi, M., Antici, P., Audebert, P., Combis, P., Fourmaux, S., Mazevet, S., Peyrusse, O., Recoules, V., Renaudin, P., Robiche, J., Dorchies, F. & Fuchs, J. 2010 "Picosecond short-range disordering in isochorically heated aluminum at solid density". *Phys. Rev. Lett.* **104**, 035 002, doi: 10.1103/PhysRevLett.104.035002

Martinolli, E., Koenig, M., Baton, S. D., Santos, J. J., Amiranoff, F., Batani, D., Perelli-Cippo, E., Scianitti, F., Gremillet, L., Mélizzi, R., Decoster, A., Rousseaux, C., Hall, T. A., Key, M. H., Snavely, R., MacKinnon, A. J., Freeman, R. R., King, J. A., Stephens, R., Neely, D. & Clarke, R. J. 2006 "Fast-electron transport and heating of solid targets in high-intensity laser interactions measured by Kα fluorescence". *Phys. Rev. E* **73**, 046 402, doi: 10.1103/PhysRevE.73.046402

Maxwell, J. C. 1860 "V. Illustrations of the dynamical theory of gases.—Part I. on the motions and collisions of perfectly elastic spheres". *The London, Edinburgh, and Dublin Philosophical Magazine and Journal of Science* **19** (124), 19–32, doi: 10.1080/14786446008642818

Maxwell, J. C. 1865 "VIII. A dynamical theory of the electromagnetic field". *Philosophical Transactions of the Royal Society of London* **155**, 459–512, doi: 10.1098/rstl.1865.0008

May, J., Tonge, J., Fiuza, F., Fonseca, R. A., Silva, L. O., Ren, C. & Mori, W. B. 2011 "Mechanism of generating fast electrons by an intense laser at a steep overdense interface". *Phys. Rev. E* **84**, 025 401, doi: 10.1103/PhysRevE.84.025401

Moiseev, S. S. & Sagdeev, R. Z. 1963 "Collisionless shock waves in a plasma in a weak magnetic field". *Journal of Nuclear Energy Part C* **5** (1), 43–47, doi: 10.1088/0368-3281/5/1/309

Mulser, P., Alber, G. & Murakami, M. 2014 "Revision of the coulomb logarithm in the ideal plasma". *Physics of Plasmas* **21** (4), 042 103, doi: 10.1063/1.4870501

Munroe, R. 2020 "Further research is needed". https://xkcd.com/2268/

Nanbu, K. 1997 "Theory of cumulative small-angle collisions in plasmas". *Phys. Rev. E* **55**, 4642–4652, doi: 10.1103/PhysRevE.55.4642

Nanbu, K. & Yonemura, S. 1998 "Weighted particles in coulomb collision simulations based on the theory of a cumulative scattering angle". *Journal of Computational Physics* **145** (2), 639 – 654, ISSN 0021-9991, doi: 10.1006/jcph.1998.6049

Nettelmann, N., Holst, B., Kietzmann, A., French, M., Redmer, R. & Blaschke, D. 2008 "Ab initio equation of state data for hydrogen, helium, and water and the internal structure of Jupiter". *The Astrophysical Journal* **683** (2), 1217–1228, doi: 10.1086/589806

Nilson, P. M., Theobald, W., Myatt, J. F., Stoeckl, C., Storm, M., Zuegel, J. D., Betti, R., Meyerhofer, D. D. & Sangster, T. C. 2009 "Bulk heating of solid-density plasmas during high-intensity-laser plasma interactions". *Phys. Rev. E* **79**, 016 406, doi: 10.1103/PhysRevE.79.016406

Nilson, P. M., Solodov, A. A., Myatt, J. F., Theobald, W., Jaanimagi, P. A., Gao, L., Stoeckl, C., Craxton, R. S., Delettrez, J. A., Yaakobi, B., Zuegel, J. D., Kruschwitz, B. E., Dorrer, C., Kelly, J. H., Akli, K. U., Patel, P. K., Mackinnon, A. J., Betti, R., Sangster, T. C. & Meyerhofer, D. D. 2010 "Scaling hot-electron generation to high-power, kilojoule-class laser-solid interactions". *Phys. Rev. Lett.* **105**, 235 001, doi: 10.1103/PhysRevLett.105.235001

Pak, A., Kerr, S., Lemos, N., Link, A., Patel, P., Albert, F., Divol, L., Pollock, B. B., Haberberger, D., Froula, D., Gauthier, M., Glenzer, S. H., Longman, A., Manzoor, L., Fedosejevs, R., Tochitsky, S., Joshi, C. & Fiuza, F. 2018 "Collisionless shock acceleration of narrow energy spread ion beams from mixed species plasmas using 1 μm lasers". *Phys. Rev. Accel. Beams* **21**, 103 401, doi: 10.1103/PhysRevAccelBeams.21.103401

PATEL, P. K., MACKINNON, A. J., KEY, M. H., COWAN, T. E., FOORD, M. E., ALLEN, M., PRICE, D. F., RUHL, H., SPRINGER, P. T. & STEPHENS, R. 2003 "Isochoric heating of solid-density matter with an ultrafast proton beam". *Phys. Rev. Lett.* **91**, 125 004, DOI: `10.1103/PhysRevLett.91.125004`

PÉREZ, F., GREMILLET, L., KOENIG, M., BATON, S. D., AUDEBERT, P., CHAHID, M., ROUSSEAUX, C., DROUIN, M., LEFEBVRE, E., VINCI, T., RASSUCHINE, J., COWAN, T., GAILLARD, S. A., FLIPPO, K. A. & SHEPHERD, R. 2010 "Enhanced isochoric heating from fast electrons produced by high-contrast, relativistic-intensity laser pulses". *Phys. Rev. Lett.* **104**, 085 001, DOI: `10.1103/PhysRevLett.104.085001`

PÉREZ, F., GREMILLET, L., DECOSTER, A., DROUIN, M. & LEFEBVRE, E. 2012 "Improved modeling of relativistic collisions and collisional ionization in particle-in-cell codes". *Phys. of Plasmas* **19**, 083 104, DOI: `10.1063/1.4742167`

PUKHOV, A. 2016 "Particle-in-cell codes for plasma-based particle acceleration". In "Proceedings of the 2014 CAS-CERN Accelerator School: Plasma Wake Acceleration", (ed. B. Holzer), vol. 1, (181–206), DOI: `10.5170/CERN-2016-001.181`

PURVIS, M. A., SHLYAPTSEV, V. N., HOLLINGER, R., BARGSTEN, C., PUKHOV, A., PRIETO, A., WANG, Y., LUTHER, B. M., YIN, L., WANG, S. & ROCCA, J. J. 2013 "Relativistic plasma nanophotonics for ultrahigh energy density physics". *Nat. Photonics* **7**, 796–800, DOI: `10.1038/nphoton.2013.217`

PUSZTAI, I., TENBARGE, J. M., CSAPÓ, A. N., JUNO, J., HAKIM, A., YI, L. & FÜLÖP, T. 2018 "Low Mach-number collisionless electrostatic shocks and associated ion acceleration". *Plasma Physics and Controled Fusion* **60**, 035 004, DOI: `10.1088/1361-6587/aaa2cc`

PUSZTAI, I., JUNO, J., BRANDENBURG, A., TENBARGE, J. M., HAKIM, A., FRANCISQUEZ, M. & SUNDSTRÖM, A. 2020 "Dynamo in weakly collisional nonmagnetized plasmas impeded by landau damping of magnetic fields". *Phys. Rev. Lett.* **124**, 255 102, DOI: `10.1103/PhysRevLett.124.255102`

QUESNEL, B. & MORA, P. 1998 "Theory and simulation of the interaction of ultraintense laser pulses with electrons in vacuum". *Phys. Rev. E* **58**, 3719–3732, DOI: `10.1103/PhysRevE.58.3719`

REMINGTON, B. A. 2005 "High energy density laboratory astrophysics". *Plasma Phys. and Control. Fusion* **47**, A191–A203, DOI: `10.1088/0741-3335/47/5a/014`

REMINGTON, B. A., ARNETT, D., PAUL, R., TAKABE, H. *et al.* 1999 "Modeling astrophysical phenomena in the laboratory with intense lasers". *Science* **284** (5419), 1488–1493, DOI: `10.1126/science.284.5419.1488`

RENAUDIN, P., BLANCARD, C., CLÉROUIN, J., FAUSSURIER, G., NOIRET, P. & RECOULES, V. 2003 "Aluminum equation-of-state data in the warm dense matter regime". *Phys. Rev. Lett.* **91**, 075 002, DOI: `10.1103/PhysRevLett.91.075002`

RINCON, F., CALIFANO, F., SCHEKOCHIHIN, A. A. & VALENTINI, F. 2016 "Turbulent dynamo in a collisionless plasma". *Proceedings of the National Academy of Sciences* **113** (15), 3950–3953, DOI: `10.1073/pnas.1525194113`

ROBINSON, A. P. L., STROZZI, D. J., DAVIES, J. R., GREMILLET, L., HONRUBIA, J. J., JOHZAKI, T., KINGHAM, R. J., SHERLOCK, M. & SOLODOV, A. A. 2014 "Theory of fast electron transport for fast ignition". *Nucl. Fusion* **54** (5), 054 003, DOI: `10.1088/0029-5515/54/5/054003`

ROMAGNANI, L., FUCHS, J., BORGHESI, M., ANTICI, P., AUDEBERT, P., CECCHERINI, F., COWAN, T., GRISMAYER, T., KAR, S., MACCHI, A., MORA, P., PRETZLER, G., SCHIAVI, A., TONCIAN, T. & WILLI, O. 2005 "Dynamics of electric fields driving the laser acceleration of multi-MeV protons". *Phys. Rev. Lett.* **95**, 195 001, DOI: `10.1103/PhysRevLett.95.195001`

ROMAGNANI, L., BULANOV, S. V., BORGHESI, M., AUDEBERT, P., GAUTHIER, J. C., LÖWENBRÜCK, K., MACKINNON, A. J., PATEL, P., PRETZLER, G., TONCIAN, T. & WILLI, O. 2008 "Observation of collisionless shocks in laser-plasma experiments". *Phys. Rev. Lett.* **101**, 025 004, DOI: `10.1103/PhysRevLett.101.025004`

ROSENBLUTH, M. N., MACDONALD, W. M. & JUDD, D. L. 1957 "Fokker-planck equation for

an inverse-square force". *Phys. Rev.* **107**, 1–6, DOI: 10.1103/PhysRev.107.1, URL https://link.aps.org/doi/10.1103/PhysRev.107.1

ROSS, M. 1981 "The ice layer in Uranus and Neptune—diamonds in the sky?" *Nature* **292** (5822), 435–436, DOI: 10.1038/292435a0

ROTH, M., JUNG, D., FALK, K., GULER, N., DEPPERT, O., DEVLIN, M., FAVALLI, A., FERNANDEZ, J., GAUTIER, D., GEISSEL, M., HAIGHT, R., HAMILTON, C. E., HEGELICH, B. M., JOHNSON, R. P., MERRILL, F., SCHAUMANN, G., SCHOENBERG, K., SCHOLLMEIER, M., SHIMADA, T., TADDEUCCI, T., TYBO, J. L., WAGNER, F., WENDER, S. A., WILDE, C. H. & WURDEN, G. A. 2013 "Bright laser-driven neutron source based on the relativistic transparency of solids". *Phys. Rev. Lett.* **110**, 044 802, DOI: 10.1103/PhysRevLett.110.044802

ROZMUS, W. & TIKHONCHUK, V. T. 1990 "Skin effect and interaction of short laser pulses with dense plasmas". *Phys. Rev. A* **42**, 7401, DOI: 10.1103/PhysRevA.42.7401

SANTOS, J. J., VAUZOUR, B., TOUATI, M., GREMILLET, L., FEUGEAS, J.-L., CECCOTTI, T., BOUILLAUD, R., DENEUVILLE, F., FLOQUET, V., FOURMENT, C., HADJ-BACHIR, M., HULIN, S., MORACE, A., NICOLAÏ, P., D'OLIVEIRA, P., REAU, F., SAMAKÉ, A., TCHERBAKOFF, O., TIKHONCHUK, V. T., VELTCHEVA, M. & BATANI, D. 2017 "Isochoric heating and strong blast wave formation driven by fast electrons in solid-density targets". *New Journal of Physics* **19** (10), 103 005, DOI: 10.1088/1367-2630/aa806b

SAWADA, H., SENTOKU, Y., YABUUCHI, T., ZASTRAU, U., FÖRSTER, E., BEG, F. N., CHEN, H., KEMP, A. J., MCLEAN, H. S., PATEL, P. K. & PING, Y. 2019 "Monochromatic 2D Kα emission images revealing short-pulse laser isochoric heating mechanism". *Phys. Rev. Lett.* **122**, 155 002, DOI: 10.1103/PhysRevLett.122.155002

SENTOKU, Y. & KEMP, A. J. 2008 "Numerical methods for particle simulations at extreme densities and temperatures: Weighted particles, relativistic collisions and reduced currents". *J. of Comput. Phys.* **227** (14), 6846–6861, DOI: 10.1016/j.jcp.2008.03.043

SHERLOCK, M., HILL, E. G., EVANS, R. G., ROSE, S. J. & ROZMUS, W. 2014 "In-depth plasma-wave heating of dense plasma irradiated by short laser pulses". *Phys. Rev. Lett.* **113**, 255 001, DOI: 10.1103/PhysRevLett.113.255001

SHOUCRI, M. M. 2011 Eulerian codes for the numerical solution of the kinetic equations of plasmas. Nova Science Publishers, ISBN 9781613245613

SILVA, L. O., MARTI, M., DAVIES, J. R., FONSECA, R. A., REN, C., TSUNG, F. S. & MORI, W. B. 2004 "Proton shock acceleration in laser-plasma interactions". *Phys. Rev. Lett.* **92**, 015 002, DOI: 10.1103/PhysRevLett.92.015002

SIMINOS, E., GRECH, M., SKUPIN, S., SCHLEGEL, T. & TIKHONCHUK, V. T. 2012 "Effect of electron heating on self-induced transparency in relativistic-intensity laser-plasma interactions". *Phys. Rev. E* **86**, 056 404, DOI: 10.1103/PhysRevE.86.056404

SKOUTNEV, V., HAKIM, A., JUNO, J. & TENBARGE, J. M. 2019 "Temperature-dependent saturation of Weibel-type instabilities in counter-streaming plasmas". *The Astrophysical Journal Letters* **872** (2), L28, DOI: 10.3847/2041-8213/ab0556

STRICKLAND, D. & MOUROU, G. 1985 "Compression of amplified chirped optical pulses". *Opt. Commun.* **56** (3), 219 – 221, DOI: 10.1016/0030-4018(85)90120-8

SUNDSTRÖM, A., JUNO, J., TENBARGE, J. M. & PUSZTAI, I. 2019 "Effect of a weak ion collisionality on the dynamics of kinetic electrostatic shocks". *J. Plasma Phys.* **85** (1), 905850 108, DOI: 10.1017/S0022377819000023

SUNDSTRÖM, A., SIMINOS, E., GREMILLET, L. & PUSZTAI, I. 2020a "Fast collisional electron heating and relaxation with circularly polarized ultraintense short-pulse laser". *Journal of Plasma Physics* **86** (2), 755860 201, DOI: 10.1017/S0022377820000264

SUNDSTRÖM, A., SIMINOS, E., GREMILLET, L. & PUSZTAI, I. 2020b "Collisional effects on the ion dynamics in thin-foil targets driven by an ultraintense short pulse laser". *Plasma Physics and Controlled Fusion* **62** (8), 085 015, DOI: 10.1088/1361-6587/ab9a62

SVEDUNG WETTERVIK, B., DUBOIS, T. C. & FÜLÖP, T. 2016 "Vlasov modelling of laser-driven collisionless shock acceleration of protons". *Physics of Plasmas* **23** (5), 053 103, DOI: 10.1063/

`1.4948424`

TAJIMA, T. & DAWSON, J. M. 1979 "Laser electron accelerator". *Phys. Rev. Lett.* **43**, 267–270, DOI: `10.1103/PhysRevLett.43.267`

THOMAS, A. G. R., TZOUFRAS, M., ROBINSON, A. P. L., KINGHAM, R. J., RIDGERS, C. P., SHERLOCK, M. & BELL, A. R. 2012 "A review of Vlasov-Fokker-Planck numerical modeling of inertial confinement fusion plasma". *J. Comput. Phys.* **231** (3), 1051 – 1079, DOI: `10.1016/j.jcp.2011.09.028`. Special Issue: Computational Plasma Physics

TURRELL, A. E., SHERLOCK, M. & ROSE, S. J. 2015 "Ultrafast collisional ion heating by electrostatic shocks". *Nat. Commun.* **6**, 8905, DOI: `10.1038/ncomms9905`

VLASOV, A. A. 1968 "The vibrational properties of an electron gas". *Soviet Physics Uspekhi* **10** (6), 721–733, DOI: `10.1070/PU1968v010n06ABEH003709`

WILKS, S. C., LANGDON, A. B., COWAN, T. E., ROTH, M., SINGH, M., HATCHETT, S., KEY, M. H., PENNINGTON, D., MACKINNON, A. & SNAVELY, R. A. 2001 "Energetic proton generation in ultra-intense laser–solid interactions". *Physics of Plasmas* **8** (2), 542–549, DOI: `10.1063/1.1333697`

YVON, J. 1935 La théorie statistique des fluides et l'équation d'état, vol. 203. Hermann & cie

ZHANG, H., SHEN, B. F., WANG, W. P., ZHAI, S. H., LI, S. S., LU, X. M., LI, J. F., XU, R. J., WANG, X. L., LIANG, X. Y., LENG, Y. X., LI, R. X. & XU, Z. Z. 2017 "Collisionless shock acceleration of high-flux quasimonoenergetic proton beams driven by circularly polarized laser pulses". *Phys. Rev. Lett.* **119**, 164 801, DOI: `10.1103/PhysRevLett.119.164801`